The Prediction and Assessment
of Weldmetal Microstructures

Martin Strangwood
King's College, Cambridge

A dissertation submitted for the degree of
Doctor of Philosophy
at the University of Cambridge, October 1987.

"What science is there in welding?"

U.S. Customs Official, Atlanta, May 1986.

Preface

This dissertation describes work done between October 1984 and August 1987 at the Department of Materials Science and Metallurgy, University of Cambridge under the supervision of Dr. H.K.D.H.Bhadeshia. Unless appropriately referenced, the work is original and is not the result of collaboration. No part of this dissertation has been previously or is currently being submitted for any degree or diploma at this, or any other, university.

This dissertation contains less than 60,000 words.

Martin Strangwood

Acknowledgements

Summary

This dissertation covers research into the quantitative phase transformation theory for low alloy steel weld deposits in three main areas:

(i) Acicular ferrite. The use of high carbon, high silicon welds allowed the γ/α phase relationship to be studied using optical, scanning electron and transmission electron microscopy. Further details of the transformation were obtained from surface relief, microanalysis and dilatometry, all of which indicated that acicular ferrite is a form of bainite.

(ii) Microphases. The presence of martensite, carbides and austenite in these regions was studied, using similar techniques to (i) and modelled on the redistribution of carbon from the pre-existing ferrite phases. This allows prediction of the microphases associated with each ferrite phase in the weld.

(iii) Nucleation of ferrite at ceramic/steel interfaces. Nucleation of ferrite on weld metal inclusions was modelled using a novel technique, based upon diffusion bonding, to create a large, planar interface area. This was then heat treated to study the formation of ferrite, the interface region was characterised by X-ray diffractometry, optical and scanning electron microscopy, microhardness, energy dispersive spectroscopy and laser induced ion mass analysis. This, and subsequent thermodynamic analyses, revealed that the dominant mechanism for nucleation of ferrite is chemical reaction between the steel and inclusion phase.

Contents

Nomenclature

The following nomenclature is widely used through this dissertation.

at%	atomic %
BSG	Bhadeshia-Svensson-Gretoft
B_s	Bainite start temperature
CCT	Continuous Cooling Transformation
CSL	Coincident Site Lattice
CS	Crystallographic Shear
EDS	Energy Dispersive Spectroscopy
$\Delta F_{Ms}^{\gamma-\alpha'}$	Driving force for martensite formation
G	Thermal gradient
$\Delta G^{\phi-\phi'}$	Driving force for transformation from ϕ to ϕ'
ΔG_i^{ϕ}	Solution free energy of i in phase ϕ
HAZ	Heat Affected Zone
HSLA	High Strength Low Alloy (steel)
IPS	Invariant Plane Strain
ILS	Invariant Line Strain
IIW	International Institute of Welding
INTER	Inclusion Nucleation TEsting Rig
K-S	Kurdjumov-Sachs
LCAO	Linear Combination of Atomic Orbitals
LFG	Lacher-Fowler-Guggenheim
M_s	Martensite start temperature
MMA	Manual Metal Arc (welding)
NP-LE	Negligible Partition Local Equilibrium
P-LE	Partition Local Equilibrium
ParaE	Paraequilibrium
PFZ	Precipitate Free Zone
ppm	Parts per million, by weight
RF	Radio Frequency
R	Solidification rate
SA	Submerged Arc (welding)
SADP	Selected Area Diffraction Pattern
STEM	Scanning Transmission Electron Microscope
SEM	Scanning Electron Microscope
TTT	Transformation Time Temperature
TEM	Transmission Electron Microscope

$T_s^{\gamma-\alpha}$	γ-α Transformation start temperature
T	Temperature
T_γ	Reaustenitisation temperature
T_{iso}	Isothermal treatment temperature
t	Time
t_γ	Reaustenitisation time
t_{iso}	Isothermal treatment time
ULCB	Ultra Low Carbon Bainitic (steel)
V_α	Volume fraction of ferrite
VDN	Vickers Diamond Number
W_s	Widmanstätten ferrite start temperature
wt%	weight percent
α	ferrite
α_{acic}	acicular ferrite
α_b	bainite
α'	martensite
α_{all}	allotriomorphic ferrite
γ	austenite
δ	delta ferrite
ε_{ij}	Wagner interaction parameter
σ	interface energy
σ_y	yield stress

In describing heat treatments the notation used is:

Upper temperature/time-Lower temperature/time

e.g. 1000°C/10 mins-500°C/300s

refers to a reaustenitisation at 1000°C for 10 minutes followed by an isothermal hold at 500°C for 300 seconds.

1. Introduction

1.1 Aim and Scope of Project

Joining processes are essential to any production technique and, of these, welding is perhaps most widespread, being used from (silicon) "chips to ships" [1]. The viability of a 'new' material may also be affected by its poor joining properties, as in some highly aligned composites. Despite the versatility of fusion welding, these joints can often act as sources of weakness in the resulting structure leading to catastrophic and spectacular failures in e.g. bridges [2], ships [3], pipelines [4] and oil rigs [5,6]. These failures are principally due to the weld metal having insufficient resistance to cleavage crack propagation at the service temperatures and loads. The expansion over the past 20-30 years of the oil and gas industries has led to the exploitation of fossil fuel deposits in ever more demanding environments, e.g. the North Sea, Alaska and Siberia. This has prompted the development of new high performance steels (Table I.1) to meet the stringent service requirements (Table I.2)[7], which may also be exaggerated by environmental attack. In conjunction with the development of wrought steels, welding processes and consumables must be improved so that the properties of the welds come close to matching those of the base materials. Previously, the evolution of welding consumables and processes has been largely empirical involving large numbers of trial welds with associated mechanical testing (e.g. Charpy impact tests) to determine the optimum composition/process combination for the desired properties. Although this should generate a sizeable database, as exists for wrought steels, commercial interests often prevent ready access to these results. In addition the empirical approach is expensive in both time and money (typically around £400,000 for each composition or process variable) and so there is a strong incentive towards systematic research aimed at the prediction of weld microstructures and properties. Once the theory governing these has been deduced, design trouble spots can be highlighted as could promising compositions or processes, thus eliminating many trial welds and much experimentation.

Programs already exist to predict weld metal microstructure with great success [8] and this dissertation describes a 3 year project to improve the accuracy and physical significance of the microstructural prediction, within a larger programme, by studying three main areas where established theory is weak.

The first of these is acicular ferrite for which no quantitative phase transformation theory exists, although its effects on toughness are generally very beneficial. Previous work on this (and other weld transformations) is first reviewed in chapter 2. The work on acicular ferrite is presented in chapter 4, chapter 3 being the verification of segregation effects on the final volume fraction of high temperature (diffusional) ferrite product phases. The solid state phase

1

transformation work is extended in chapter 5 to the final products - microphases - and the relation between these and the earlier formed phases. The final toughness may depend on whether Widmanstätten ferrite has martensite, retained austenite or carbides between the plates and which phase is then associated with acicular ferrite.

The final area investigated is that of nucleation at steel/inclusion interfaces in order to determine the role of:

(a) oxide inclusions on the initial austenite(γ)-ferrite(α) transformation temperature, a parameter that could control the amount of allotriomorphic ferrite present.

(b) the potency of different ceramic phases on the nucleation of ferrite in the acicular ferrite transformation temperature range.

This is important in order to maximise the beneficial microstructural effects whilst reducing sites for void and crack nucleation. This work is contained in chapters 7-9 after a review of inclusion effects in chapter 6.

Table I.1. High strength/toughness pipeline steels.

	Alloy Contents (wt%)						
	C	Mn	Si	S	Nb	Ti	B(ppm)
HSLA	0.05	1.50	0.05	0.006	0.04-0.07	-	-
ULCB(X80)	0.01-0.03	1.50-2.0	0.05	<0.005	0.04	0.01	10

Table I.2. North Sea service conditions.

Wind speeds	$50ms^{-1}$ (110mph)
Wave height and frequency	1m at 0.1Hz, upto 30m every 50 years
Temperature	5°C (seabed) to 15°C (surface)
Sea bed pressure	17 atmospheres
Design stress	60 MNm^{-2}
Projected Life	30 years

2. Microstructural Development in Ferrous Weld Deposits

2.1 Fusion Welding

The joining of two components by fusion welding processes involves the passage of an energy source (flame, electric arc, laser or electron beam) along the joint line. The energy supplied by the source causes regions of the components under it to melt and form the weldpool. A filler metal and flux may also be added as a consumable electrode or a separate wire may be fed into the weldpool and these are also melted into the weldpool, where the majority of alloying and deoxidation occurs. This work is mainly concerned with arc processes: manual metal (MMA) or submerged arc (SA), which have an arc between the joint and an electrode (fig. 2.1) as the energy source. This region can reach temperatures of $\approx$ 20,000K, generating a plasma state between the arc and the workpiece in which the flux and filler decompose and vapourise. Some of the elements in the plasma will be lost to the atmosphere, but the rest are transferred to the weldpool. In addition, droplet transfer across and around the arc can also take place. The alloying of the weld metal is therefore achieved through the flux composition, as the filler wire is generally mild steel. If the arc was stationary the weldpool would be hemispherical, but the forward motion of the arc causes it to be elongated into a teardrop/ellipse shape. Surrounding the weldpool is a region whose temperature is raised, but not sufficiently to cause melting although some solid state transformations, such as precipitate dissolution, coarsening, grain growth and $\alpha \rightarrow \gamma \rightarrow \alpha$ transitions can take place, during the thermal cycle. This heat affected zone (HAZ) varies in extent with heat input, controlled by arc voltage and travel speed. After passage of the arc, the weldpool cools very rapidly as it is small and surrounded by a large heat sink and undergoes the following transformations:

(i) Solidification of the weldpool as primary austenite (γ) or delta (δ).

(ii) Formation of γ - if this is not the primary solidification phase.

(iii) Decomposition of γ into various kinds of ferrite phases.

The majority of work has concentrated on (iii) as this has the largest effect on final mechanical properties, but this stage will also be influenced by (i) and (ii).

2.2 Weldpool Solidification

Solidification in castings is well understood in terms of the formation of chill, columnar and equiaxed zones [9] under the influence of a reasonably constant temperature gradient. Reviews of weld solidification[10,11] have attempted to draw analogies with casting (Table II.1). The situation in welding is complicated due to the movement of the arc so that melting, mixing and freezing occur at different points within the same pool and the direction of maximum heat flow varies

with time during solidification, so that the simplified one dimensional approximations valid for ingot solidification do not always hold for welding situations.

The initial solidification occurs on the melted back HAZ of the base plate, whose grains provide preexisting nuclei, fulfilling the role of the chill zone in casting. No nucleation stage is involved so that growth initiation does not have a significant activation barrier and continuity of grains exists across the HAZ/fusion zone interface [12,13]. The epitaxial nature of this process means that growth would generate weld metal grains in the same crystallographic orientation as the immediately contiguous parent-plate grains across the fusion zone/HAZ interface. The use of Laue back reflection X-ray techniques has allowed the crystallographic orientation to be measured either side of this interface and has confirmed the relationship predicted above for many metals [13,14,15,16]. There will therefore be a dependence of initial solidification grain size, i.e. width at the base of the columnar grains, and orientation upon the texture and grain size of the HAZ [12,15,17]. HAZ grain size and texture will itself be influenced by the starting base plate microstructure. Attempts at the prediction of HAZ grain size for certain systems where precipitates limit austenite grain size (Nb, V and Ti HSLA steels) have given encouraging results [18]. However, these have not yet been extended to an accurate prediction of initial solidification grain size in the weld metal itself. As the extent of the HAZ varies with weld thermal cycle, this would be expected to influence the initial solidification structure, but this is not always observed [15,17], especially at low heat inputs, where HAZ grain growth is limited. A further complication exists due to incomplete melting and mixing, Savage and Szekeres [19] found that the fusion boundary is not precisely coincident with the point where complete melting has occurred. Therefore, regrowth of the solid can initiate within regions of the HAZ that have not completely melted and mixed with the main body of the weld pool. Use of electron microprobe analysis [20,21], reveals a region of incomplete mixing 80-150μm in width at the edge of the fusion zone in steel weldments. The width of the incompletely mixed zone would be expected to vary with heat input, travel speed and degree of segregation in the baseplate. The last factor arises because segregation of alloying elements especially S and P to grain boundaries combined with the greater energy of these defects results in liquation of grain boundaries at lower temperatures than the grain centres, i.e. further into the baseplate.

Solidification proceeds with the fastest growth direction (<100> for body centred cubic (BCC) and face centred cubic (FCC) crystals) parallel to the maximum thermal gradient (as in the columnar zone of castings). This gradient is always normal to the solid/liquid interface and its direction at any point varies continuously after passage of the arc. The HAZ grains will not all be suitably oriented for columnar growth so that competitive growth between suitably (fast) and non-suitably (slow) oriented grains leads to a predominance of the former over the latter and a reduction in the number of grains away from the HAZ/fusion zone interface [16,22]. The theory for this preferential orientation and competitive growth has been developed with respect to ingot solidification and, under certain conditions, can be applied to weld pools. This accounts for the

poor correlation between fusion and HAZ grain sizes. The variation of thermal gradient is responsible for the dependence of solidification structure on weldpool shape and hence on heat input and travel speed.

Crystal growth rate is determined by the need to maintain a constant weldpool shape (fig. 2.2). Assuming crystal growth is parallel to the maximum thermal gradient then

$$R = V\cos(\theta) \qquad \qquad .....(1)$$

where

R=local solidification rate at a point on the solid/liquid interface

V =welding speed

θ=angle between welding direction and the direction of the maximum thermal gradient at the point on the interface

As solidification occurs along a fast growth direction, which is not necessarily parallel to the maximum thermal gradient, but at θ′ to the welding direction [12], the local solidification rate is:

$$R = V\cos(\theta)/\cos(\theta'-\theta) \qquad \qquad .....(2)$$

as illustrated in fig. 2.2b.

At low travel speeds (fig. 2.3a) the weldpool is elliptical in shape so that the change in direction of the maximum thermal gradient takes place gradually and the crystals are able to follow it to give curved grains [12,23]. The curvature is achieved by repeated sidebranching of the solidification substructure [22,25] although the crystallographic orientation is constant. These welding speeds allow more grains to survive to the bead centre, renucleation being necessary at high curvatures (greater than that achievable by branching) and this may lead to a more equiaxed centreline structure. By contrast, there is little curvature at high travel speeds (fig 2.3b) where a tear shaped weldpool exists. The maximum thermal gradient is constant for a substantial part of the solidification time allowing favourably oriented grains to develop at the expense of non-favourable orientations. The resulting grain structure is much straighter with much fewer grains surviving to the centreline.

2.2.1 Variations in Growth Mode

Unlike ingot solidification, welds seldom exhibit a transition from a columnar to an equiaxed structure. A refined, equiaxed grain structure being less prone to solidification cracking, is preferred although it may give rise to a greater amount of grain boundary nucleated allotriomorphic ferrite. The absence of an equiaxed structure is due to the very severe thermal conditions in the melt which make nucleus survival unlikely, so that the equiaxed structure cannot nucleate and grow to block development of the columnar grains. The possible nuclei (e.g. fragmented dendrite arms, innoculants, and surface grains - usually absent in submerged arc welding due to the insulating flux layer) remelt too rapidly to provide equiaxed grains. Generally the weldpool volume is small compared to the surrounding components, which act as a huge heat sink, and, along with small heat input, give rise to very large thermal gradients and rapid cooling.

Under conditions of very high cooling rates, achieved by use of extremely high welding speeds [26,27], welding of thin sheets [28], high alloy content [19,20] or by enhanced surface cooling a dendritic substructure is extensively stimulated and equiaxed structures nucleated on dendrite fragments have been observed. Enhanced surface cooling [29], when argon jets were played onto the weldpool surface ahead and behind the arc, provided crystal fragments for nucleation in the later stages of solidification, akin to comet grains in castings [30]. Some grain refinement was achieved, but this was dependent on the overall welding conditions (fig. 2.4). The use of high welding speeds eg 1 mm/min for 1 mm thick steel sheet [28] give very long tear shaped weld pools with overlapping of regions of solute accumulation along the centreline which provides suitable conditions for growth of fragments ahead of the solid/liquid interface. The use of inoculants e.g. TiC [29] has been studied, TiC being found to cause refinement of the solidification structure when introduced at the trailing edge of the weldpool, an effect similar to that observed for steel ingots [9,31]. The refinement depended upon the rate of inoculant addition, with a minimum critical feed rate necessary for refinement to occur, presumably in order to provide sufficient nucleation sites in the weldpool. Inoculant size was also important with smaller sizes being more effective than larger ones due to the higher number of nucleating sites available for the same inoculant feed rate. There will be a lower limit to effective inoculant size when (a) the particles melt before nucleating and (b) they are below the critical radius for nucleation. If heat input is increased then the inoculant efficiency is reduced as slower cooling causes some innoculants to be swept into the hotter regions of the weldpool where melting can take place. In addition limited grain refinement can be achieved by current modulation, arc weaving, vibration and ultrasonics [10], but their efficiency is again altered by overall welding conditions. Generally the result of weld solidification is a large (100μm x 3000μm)[9] columnar grain structure with a dominant <100> texture of primary γ or, more commonly for low alloy steels, δ.The actual primary phase found depends on alloy content and cooling rate.

The chill and equiaxed macrostructural zones are absent from the majority of welds, but the full range of substructures - planar, cellular and dendritic - are observed at various stages of solidification, as the combination of growth rate, thermal gradient and constitutional supercooling changes [32]. Studies of ingot solidification have revealed three regions of interface stability (fig. 2.5). Referring to the phase diagram, fig. 2.6, if the solute equilibrium partition coefficient (k_0), i.e. the ratio of solute in solid to that in liquid at the same temperature, is less than one, then upon solidification solute is rejected into the remaining liquid where it diffuses away. This redistribution takes a finite time resulting in a solute concentration profile ahead of the solid/liquid interface (fig. 2.5) [33],

$$C = C_0 \left\{ 1 + \frac{(1-k_0)}{k_0} \exp(-Rx/D) \right\} \qquad \text{.....(3)}$$

C=solute concentration at distance x into the liquid from solid/liquid interface

C_0=bulk concentration

x=distance into liquid from the solid/liquid interface

D=diffusivity of solute in liquid

R=crystal growth rate, i.e. local solidification rate for poorly stirred solutions where convection is limited, so that solute redistribution is by diffusion in the liquid.

This causes the liquidus temperature to vary away from the interface in a manner consistent with the phase diagram. The profile can now be replotted as a liquidus profile (fig. 2.5), according to the equation [33]:

$$T_L = T_i + mC_0 \frac{(1-k_0)}{k_0} \{1 - \exp(-Rx/D)\} \qquad \text{.....(4)}$$

T_L=liquidus temperature

T_i=liquid temperature at the interface

m=slope of the liquidus on phase diagram

The actual temperature (T) of the melt is given by

$$T = T_i + Gx \qquad \text{.....(5)}$$

G=thermal gradient in melt

where

$$T_i = T_m - mC_0/k_0 \qquad \text{.....(6)}$$

T_m=melting temperature of the pure metal

Various thermal gradients G can be superimposed upon this plot of the variation of liquidus temperature away from the solid/liquid interface, fig. 2.5. If G is the thermal gradient in the melt as imposed on the system and R is the growth rate of the solid then at high G/R the liquid temperature is always above the liquidus and no supercooling ahead of the interface occurs. The advance of the interface will be equal at all points along its surface as any perturbations will be remelted by the liquid resulting in a planar interface. With reduced G or increased R then G/R cuts the liquidus profile at the interface and at λ so that the liquid between these points is at a temperature below its liquidus and is *constitutionally supercooled*. Any perturbation in the planar interface now projects into metastable liquid and is stabilised to a distance λ. If λ is small and R is not great then these perturbations will nucleate rapidly, but will grow more slowly so that the interface degenerates into a series of cells (fig. 2.7) and the resulting growth is *cellular*. Further reductions in G or increases in R greatly increase λ, so that perturbations develop to a large extent with growth and sidebranching of an existing perturbation occuring more rapidly than the nucleation of an adjacent perturbation. The substructure is then dominated by fewer tree-like dendrites, which may retain a cellular nature overall (cellular-dendritic) or give a fully dendritic growth mode [11]. The various G/R regimes have been analysed by Savage [11] on the basis of

8

Tiller and Rutter's [34] solution for ingot solidification under certain growth modes:

$$G/R > \Delta T/D \qquad .....(7)$$

For planar growth, where ΔT is the interval between liquidus and solidus temperatures and D is the diffusivity of the solute in the liquid. Cellular-dendritic and fully dendritic growth results [36] if:

$$G/R < \Delta T/D \qquad .....(8)$$

Relating this to the travel speed V from equation 2, this becomes:

$$G\cos(\theta'-\theta)/V\cos(\theta) < \Delta T/D \qquad .....(9)$$

Although this expression is widely used for describing weld solidification, it has no theoretical foundation, which limits its quantitative usefulness.

During weld solidification, the initial solidification is planar as convection in the weld pool rapidly redistributes solute, but readily gives way to a cellular form, as the arc moves away so that the contribution of convection is reduced with respect to diffusion. These cells are generally hexagonal in section [11], fig. 2.8, and persist during most of the solidification. Cellular-dendritic (irregular globular sectioned) cells, fig. 2.8, are present in the centre of the weld during solidification, where temperature gradients are at their smallest and segregation at its highest level (i.e. ΔT is maximised). This substructure is promoted by the use of high heat input or fast welding speeds, even to the extent of equiaxed grains. The use of highly alloyed systems (beyond the scope of this work) increases the level of partition and results in larger values of ΔT, which enhances cellular/dendritic transformation as shown by welding of two different composition baseplates [36], fig. 2.9. This regime is important in high toughness (generally high [Ni]) welds as the substructure affects segregation behaviour and inclusion distribution.

2.3 Chemical Segregation Effects

During solidification of multicomponent systems, solute redistribution occurs ahead of the solid/liquid interface resulting in compositional inhomogeneities (segregation) in the final solid. Two classes of segregation exist; microsegregation (extending over a distance of one grain diameter or less) and macrosegregation (extends over several grain diameters). The short range effects often occur during cellular mode with solute accumulation (if $k_0 < 1$) in the liquid enriching grain and cell boundaries (fig. 2.10) [10]. This generally produces large compositional variations, which can be removed in castings by subsequent solution treatments. In welds, however, this is not practicable and the microsegregation remains, exerting a strong influence on microstructure and properties. Coring and interdendritic solute enrichment are common during dendritic growth and are much more difficult to remove. The segregation would be present towards the centreline of a weld and can influence the distribution of low melting point inclusions (e.g. silicates). The centreline region also exhibits macrosegregation where the solidification fronts from either side of the weld impinge, trapping a solute rich layer of liquid between them (fig. 2.11). The action of thermal stresses, as the solid cools and contracts, on this low melting point liquid, generally

containing relatively high levels of S and P, causes it to collapse to leave *solidification cracks*. As solidification proceeds from HAZ to centreline then the solid deposited gradually increases in solute content; a gradient results which diffusion in the solid is too slow to remove. This is the general form of macrosegregation, although in welding it is further complicated by dilution of the outer weldment material by melting of the adjacent baseplate, causing another compositional heterogeneity. The exact pattern of segregation depends on growth conditions and morphology, especially fluid flow through dendritic (semi-solid) regions as these can cause remelting and channel formation in which the final solute rich liquid can solidify. Alternatively, the trapping of solute enriched liquid in interdendritic spaces gives rise to strong segregation over short interdendritic spacings (<10μm) and variation in inclusion distributions [37].

The presence of segregation in weld deposits gives rise to variations in mechanical properties and weld defects, which are more developed than in castings because of the faster cooling and reduced opportunity for solution treatment (usually limited to a stress relief heat treatment). Despite its very great effects, the quantitative study of segregation in weld deposits is not well reported. One reason for this is the fine substructure scale which often limits the use of electron probe microanalysis. Despite this, solute-rich layers ahead of the solid/liquid interface have been observed [38] and, by developing and studying back filled cracks, the equilibrium distribution coefficients have been measured. The cracks were developed by bending a joint as welding was performed, so that cracks were formed at the grain boundaries in the non-melted baseplate and molten metal from the weldpool adjacent to the solid/liquid interface adjacent to these cracks flowed into them [39]. These agree closely with those reported for ingot solidification suggesting that the same base mechanisms operate in both cases.

Superimposed on this segregation is solute banding (alternate solute-rich and solute-depleted regions) and surface rippling. The former can be observed as light and dark lines on an etched weld section and arises due to variations in the solidification rate which cause solute dumping or absorption (fig. 2.12). Direct correlations between ripples and banding [40,41] and solidification substructure periodicity [41] directly relates molten pool disturbances with solidification behaviour. The frequency of the ripples also corresponds to that of the power source so that these effects can be attributed to changes in arc stability and/or characteristics every cycle causing alternating increases and decreases in interface temperature and consequent retardations and accelerations of the solidification front.

The similarity between segregation in casting and welds allows the latter to be modelled from the extensive data that exists for the former. Hence elements such as Mn, S, P and Si will enrich the liquid and the initial solidification grain and cell boundaries, if the initial phase is δ these are then the γ grain centres. In this case the γ grain boundaries are denuded in solute and transform much more rapidly to ferrite; the reverse occurs if γ is the primary phase where the γ grain boundaries are enriched in solute so that ferrite formation is retarded. Further work by Flemings et al. [42-44] and Fredriksson and co-workers [45-48], illustrated the importance, not only of the solute

10

partition coefficient k_0, but also of diffusion in the solid phase. As the diffusivity of solute in the solid decreases then redistribution takes place less readily and the degree of segregation increases. In iron-based systems, the diffusivity of elements in δ can be up to 100 times that in γ leading to a much higher degree of segregation if γ is the primary solidification phase.

Thus accurate prediction of the primary solid phase is essential to the subsequent microstructural development and properties. The Fe-C phase diagram predicts that δ would be the primary phase completely up to 0.09wt%C, from 0.09-0.53wt%C δ forms first, then γ as the remaining liquid undergoes a peritectic reaction with the preexisting δ. Above 0.53wt%C, the initial solid would be γ up to the eutectic at 4.30wt%C, with no δ [49], fig. 2.13. However, Fredriksson illustrated the importance of cooling rate by solidifying a Fe-0.1C-1.5Mn-0.4Si wt% alloy as primary γ at welding speeds of 100cmmin^{-1}, when the phase diagram would predict primary δ formation [47,48]. The effect of substitutional alloying elements was found to be negligible compared with that of carbon content. This corresponded to the cooling curve crossing the extended γ liquidus and reaching a temperature at which:

<center>Growth rate of austenite > Growth rate of delta</center>

before δ had time to nucleate. This could be achieved at typical welding cooling rates, but the low carbon levels used to avoid excessive hardness still tend to give nucleation as primary δ. The lack of any significant nucleation barrier to solidification confuses the analysis as epitaxy may be important with the HAZ structure determining the initial phase. This structure, near the melting point can only be varied by changes in alloying, which will alter the weld metal composition by dilution so that the effects of base plate microstructure and chemical composition cannot be determined independently. The variation of initial phase for low alloy ferrous welds has been predicted by Bhadeshia and co-workers , fig. 2.14 [50], assuming equilibrium partition of alloying elements between solid and liquid. From that the γ liquidus can be extended using low alloy thermodynamics based on Wagner interaction parameters [51].

The spatial segregation of inclusions will be dealt with in chapter 6.

2.4 Austenite Formation

Studies on the formation of austenite from δ are sparse compared with those on its decomposition to the various ferrite phases. Recent work [52] using Al as an alloying element has managed to capture the initial stages of the δ-γ transformation (fig 2.15). This clearly indicates the nucleation of γ on the prior δ grain boundaries. Interfacial energy, fast diffusivity and collector plate action then promote anisotropic growth along the boundary in preference to normal to it. This results in a columnar γ grain structure resembling that of the original δ-ferrite, but whose size may be smaller [53] or larger [54] than the original δ. The size will be determined mainly by a balance of two factors:

(i) initial nucleation rate on the δ grain boundaries, before the allotriomorphs impinge to give a continuous boundary film;

<center>11</center>

(ii) inclusion hindrance of the migrating austenite boundaries.

As oxide particles generally form ahead of the solid/liquid interface they can interact with it as it moves up to them. This interaction tends to push the inclusions along the interface to accumulate at solidification boundaries [55,56]. Barritte [57] analysed the critical free energy for nucleation at an inclusion compared with a grain boundary and found that the latter was more favourable, for the same chemical driving force. Therefore, despite the accumulation of inclusions at solidification boundaries, these will not directly affect nucleation of γ at these sites. The nucleation rate will be determined by alloying (chemical driving force) and original δ grain size (i.e. number of sites available), which is dependent upon HAZ grain size, texture and welding conditions. The effect of inclusion pinning, point (ii), is not clear in the as-deposited structure and is dealt with more fully in chapter 6. Once nucleated, the γ grains will grow rapidly by diffusion at these elevated temperatures and adopt a morphology similar to that of the original δ grains, presumably through preferential growth parallel to maximum thermal gradient, $\underline{\nabla}T$, and/or along the grain boundaries through the latter's interfacial energy, faster diffusivity and collector plate action. However, they may not correspond exactly as, during their growth, the arc has moved further away so that the direction of the maximum thermal gradient present during γ formation is not parallel to that present during δ solidification, fig. 2.16 [58].

2.5 The Austenite - Ferrite Transformation

2.5.1 Nomenclature

The decompositon of γ under continuous cooling, and the variety of sites available for ferrite (α) nucleation gives rise to a number of ferrite morphologies at room temperature. The sizes, compositions and proportions of these phases to a large extent control the mechanical behaviour of the weld in service.

Although a large amount of research has been undertaken on the microstructure and mechanical properties of welds, correlation of results between different workers is often difficult, because of the preponderence of nomenclature schemes. Unlike wrought steels, where the Dubé classification [59], fig. 2.17, is fairly universally accepted and applied, until recently welding research did not have a single adopted scheme but several catering for the different tastes of their originators. In the UK some of these attempted to relate microstructure with:

(i) Toughness [60]. This scheme used four constituents, proeutectoid ferrite, lamellar products, acicular ferrite and others. This has some ambiguity, e.g. Widmanstätten α plates, one of the lamellar products, could also be classed as proeutectoid ferrite. The structures correlate reasonably with toughness measurements, but cannot deal with the wide range of welding microstructures, which determine other properties.

(ii) Dubé classification [61]. Three of these constituents were used, namely allotriomorphic ferrite, ferrite sideplates and intragranular 'sideplates'. Although this tries to relate weld and wrought steel microstructures the number of constituents is too limited to describe fully

allotriomorphic structures or to distinguish primary and secondary sideplates.

(iii) Identification based on morphology using optical microscopy [62]. This was devised to allow ready quantification of weld microstructures, without specialised equipment, on the basis of six categories; grain boundary ferrite, polygonal ferrite, acicular ferrite, ferrite with aligned martensite/austenite/carbides (M-A-C), ferrite-carbide aggregate (including pearlite) and martensite. These should all be resolvable optically, although martensite may require high magnifications and picral etches, but the various microphase constituents (M-A-C) are not easily distinguished nor does the scheme give any idea of transformation mechanism.

Of these (iii) is the most widely used and has been adopted with modifications by the International Institute of Welding (IIW); the various schemes are summarised in Table II.2 and typical microstructural features in fig 2.18. In addition, numerous purely descriptive schemes exist, e.g. Ito & Nakanishi [63], whose fine feathery ferrite corresponds to acicular ferrite. Another Japanese scheme [64], relates the phases to their transformation mechanism and so is more scientifically valid; it is, however, more difficult to apply and hence less widely used.

The development of a welding microstructure will therefore be considered on the basis of the IIW scheme with modifications where necessary to illustrate the transformation mechanism. Each of the ferrite phases will be reviewed with particular attention to their transformation behaviour and modelling, the development of the series of ferrite products being schematically illustrated in fig. 2.19.

2.5.2 Allotriomorphic Ferrite (Grain Boundary or Pro-eutectoid)

Examination of weld microstructures often reflects the presence of a grain boundary phase whose shape does not indicate its crystal structure - allotriomorphic ferrite. The other terms, grain boundary or pro-eutectoid ferrite, are too general as they can include Widmanstätten α, whose transformation mechanism differs considerably from that of allotriomorphic ferrite. This is the first ferrite phase to form, nucleating between 910°C and 600°C depending on alloy content and cooling rate, as indicated by quenching experiments [65]. These experiments indicated prior γ grain boundaries decorated by a layer of allotriomorphic ferrite, whilst the grain interiors were untransformed down to the martensite start temperature. The temperature of formation and shape suggest a diffusional transformation product, which, due to the low driving force, generally saturates the grain boundaries rapidly, also shown by ref. 66. Further growth is accomplished by the unidirectional motion of the α/γ interface normal to itself. This phase is then directly analogous to grain boundary nucleated ferrite in wrought steels, the thermodynamics and kinetics of whose nucleation and growth are well known and accurately modelled [67-77]. This has recently been reviewed by Bhadeshia [78].

Nucleation occurs on boundaries to form spherical caps or pillboxes, the latter minimising surface energy and may be preferred at lower driving forces [79,80], often with one interface adopting a rational (low interface energy, σ) orientation relationship with the adjacent γ (fig 2.20). The adoption of one low energy interface often precludes the adoption of a second one

13

with the other neighbouring grain, so that preferential growth into the first grain (fig. 2.21) takes place, resulting in facetted allotriomorphs on the grain boundary. Various predicted transformation-temperature-time (TTT) curves [81], based on separate C curves for diffusional and displacive transformations, show great accuracy in predicting incubation times to nucleate diffusional ferrite. However, the nucleation of allotriomorphic ferrite in low alloy welds is generally so rapid that this factor can often be neglected. As higher alloy welds are studied then this may change, but the data and models exist to incorporate this factor. Other predictive programs [82] based upon a single C curve, are limited to dilute alloys and underestimate the effect of elements such as molybdenum, which develop the 'bay' between diffusional and displacive C curves. In the dilute alloy regime the two C curves overlap and can be approximated to a single curve.

Growth of allotriomorphic ferrite is very important to microstructural prediction as this determines the volume fraction of γ available to form the other phases and the C enrichment of the remaining γ that has occurred. Hence any error in the volume fraction of allotriomorphic ferrite (V_α) will be magnified through the rest of the calculation. An accurate knowledge of the factors controlling V_α is necessary, as too large a volume fraction is associated with poor toughness [83,84]. The large width of allotriomorphic α allows cracks to develop to a large size so that at low service temperatures propagation of these defects occurs readily. Fortunately, numerous studies on diffusional formation of ferrite mean that the dominant mechanisms, their rates and the alloy/temperature regimes in which they act are well known e.g. see ref. 78. These have highlighted four main growth modes.

2.5.2.1 Diffusional Growth

Alloying elements in steel can be classified as substitutional, slow diffusers requiring vacant lattice sites, and interstitial, fast diffusers that occupy the sublattice of interstices, and either or both can control growth rate depending on driving force.

(i) Partition-Local Equilibrium (P-LE)

At low driving forces only small deviations from equilibrium can be tolerated at the interface (as for binary alloys) for both substitutional and interstitial elements. Long range diffusion of the substitutional alloying element(s) takes place, which must keep pace with the faster diffusing interstitial element (often carbon), subject to local equilibrium at the interface. This arises because the independent mass balances for each element must be compatible with a single interface velocity; these mass conservation conditions are given by[85]:

$$J_1 = -D_{11}\nabla C_1 - \sum_j D_{1j}\nabla C_j \qquad \qquad .....(10)$$

$j \neq 1$

J_1 = flux of carbon in austenite at the interface

D_{11}=diffusivity of carbon in austenite

C_1=carbon concentration

D_{1j}=ternary diffusion coefficient for the effect of element j on carbon flux

C_j=concentration of element j

for carbon and for the substitutional alloying elements

$$J_j=-\sum_k D_{jk}\nabla C_k - D_{jj}\nabla C_j \qquad .....(11)$$

$j\neq1 \quad k\neq j$

J_j=flux of element j

D_{jk}=ternary diffusion coefficient between elements j and k

In general, the only significant ternary diffusional interaction is that of substitutional alloying elements upon the diffusion of carbon, so that (11) simplifies to:

$$J_j=-D_{jj}\nabla C_j \qquad .....(12)$$

Conservation of mass can then be defined at the interface, s^*, for a ternary system as:

$$(C_{ip}-C_{im})ds^*/dt = -J_i\big|_{s=s^*} \qquad .....(13)$$

where the subscripts p and m refer to precipitate and matrix respectively.

Because of the great difference in diffusivities of the two types of element, then (13) is satisfied by reducing the driving force for diffusion of carbon almost to zero [85], fig. 2.22. The tie-line defining the interface composition and controlling the growth rate is not that passing through the bulk composition, as this must lie on the carbon isoactivity line. The interface tie line is defined as that which terminates at the interception of the isoactivity line through the bulk composition and the $(\alpha+\gamma)/\gamma$ phase boundary (fig. 2.22). This reduces the flux of the interstitial element to that of the substitutional, which now partitions between parent and product phases. This partition of the substitutional element gives a generally slow growth rate. The growth rates for various shape preserving particles (e.g. spheres, cylinders and ellipses) can then be calculated from [70-72]:

$$ds^*/dt = 0.5\eta_2 \ (D_{22}/t)^{0.5} \qquad .....(14)$$

η=growth rate constant defined by:

$$s^*=\eta_1\sqrt{(D_{11}t)}=\eta_2\sqrt{(D_{22}t)} \qquad .....(15)$$

The subscript 2(=j) refers to the substitutional alloying element, for carbon j=1.

From the tie line C_{1m}, C_{2m}, C_{1p} and C_{2p} defining growth rate are obtained and hence:-

$$f^k_2 = (C_{2b} - C_{2m})/(C_{2p} - C_{2m}) \qquad .....(16)$$

f^k_i are the fractional compositions for various precipitate morphologies (k=s, spherical; c, cylindrical; p, planar) and relate matrix concentration distributions and growth rate for these morphologies.

Subscript b refers to the bulk composition.

Then from fig. 2.23 or Table II.3, η_2 can be obtained, as:-

$$f^k_2 = f^k(\eta_2)$$

.....(17)

(ii) Negligible Partition-Local Equilibrium (NP-LE)

As driving force increases then a second mode of ensuring parity of substitutional and interstitial element fluxes can occur. This is achieved by increasing the former's driving force effectively to infinity, resulting in negligible partition between the phases and low diffusional drag. This occurs by maintaining the substitutional element concentration in α very close to the bulk value, which lies on that element's isoactivity line. Unlike the effect of substitutional elements on the activity of e.g. carbon, the effect of the interstitials on the activity of the substitutional element's activity is very small, so that the isoactivity lines are effectively parallel to the interstitial axis (fig. 2.24). The generally low driving force still means that equilibrium is maintained at the interface for both types of elements, but the substitutional element achieves equilibrium by a "spike" at the interface. This spike requires short range diffusion in the region of the interface but removes the need for long range diffusion of the substitutional element. Again the tie-line does not go through the bulk composition, but terminates at the intersection of the substitutional element isoactivity line (through the bulk value) and the $(\alpha+\gamma)/\alpha$ phase boundary. The growth equations are now given by [70-72] :

$$ds^*/dt = 0.5\eta_1 \ (D_{11}/t)^{0.5}$$

.....(18)

Ternary diffusional interactions mean that:

$$f^k_1 \neq f^k(\eta_1)$$

.....(19)

instead, under NP-LE conditions

$$f^k_1 = f^k(\eta_1) - mD_{12}/D_{11}\{1 - f^k(\eta_1)\}$$

.....(20)

$$m = (C_{2p} - C_{2m})/(C_{1p} - C_{1m})$$

.....(21)

The tie line gives C_{1m}, C_{1p}, C_{2m}, C_{2p} and hence m, so that η_1 can again be found from fig 2.23. Irreversible process thermodynamics [86,87] give

$$D_{12}/D_{11} = \varepsilon_{12}N_1/(1 + \varepsilon_{11}N_1)$$

.....(22)

as a function of mole fraction of carbon, N_1.

ε_{ij} are the Wagner interaction parameters for elements i and j.

The phase diagram can now be separated into two regions (fig 2.25), one where P-LE dominates at low supersaturations and NP-LE at high supersaturations. Both of these mechanisms are affected by soft impingement (interaction of diffusion fields), which reduces the activity gradient and hence the growth rate. This is manifested as a shift in the tie-line defining the interface towards the bulk composition, through which it passes when reaction ceases.

(iii) Paraequilibrium (ParaE)

Increases in driving force and growth rate over NP-LE cause a further change in growth mode, as interface equilibrium is abandoned. This may arise as the "spike" decreases in width as growth rate increases until it is less than a lattice spacing. This situation is only possible mathematically

[70-72]. In this case there is no change in substitutional alloying element concentration across the interface (fig. 2.26), it being too slow to diffuse even within the short range of the "spike". The resulting tie-line is therefore parallel to the interstitial element axis and is a component ray of these elements. The latter, by virtue of their rapid diffusion, are able to redistribute and so that equilibrium *with respect to these elements*, is maintained across the interface, subject to the constraint of constant solvent/substitutional element ratio. This paraequilibrium situation was first suggested by Hultgren [88,89]. The interstitial element again controls the growth rate, but the added constraint ensures that this is the fastest growth mode, the rate being given by:

$$ds^*/dt = 2D_{11}/\Delta s \qquad \qquad .....(23)$$

where Δs is the "spike" width, which is estimated using a Zener approximation [90] to estimate the diffusion zone thickness, with mass conservation becoming:

$$V_P(C_{2p}-C_{2b}) \approx 0.5A_P\Delta s(C_{2b}-C_{2m}) \qquad \qquad .....(24)$$

V_P=precipitate volume

A_P=precipitate area which leads to

$$\Delta s/s = \phi(1/f_2-1) \qquad \qquad .....(25)$$

s=appropriate characteristic precipitate dimension, eg radius for spheres

ϕ=2(planar), 1(cylindrical), 2/3(spherical).

Although the width of the "spike" can be calculated, experimental verification is lacking and prediction of when the "spike" width is ≤a, i.e. when NP-LE should become ParaE, does not accurately chart the trend [91]. Therefore, the theory, advanced as it is, requires more work in this area. Somewhat arbitrary limits have been set on "spike" width [70] with:

$$\Delta s > 50Å \quad \text{Local Equilibrium}$$
$$\Delta s < 10Å \quad \text{Paraequilibrium}$$

These growth rates represent extreme cases and also neglect factors such as soft impingement, which causes the tie line shift towards the bulk tie line.

(iv) Interface Control

During diffusion controlled growth, the driving force is largely dissipated in long range solute diffusion ahead of the interface. However, in some cases, e.g. a highly ordered singular interface, the driving force is dissipated in atom transfer across the interface, which becomes the rate controlling step. In the extreme case, transfer of atoms across the interface is much slower than diffusion of them to or from the interface and so there is virtually no matrix concentration gradient away from the interface (fig. 2.27a). More often, however, growth occurs under mixed interface and diffusion control (fig. 2.27c). In alloys, under interface control, local equilibrium is not maintained at the interface [78] so that the chemical potential of one or more elements is discontinuous. The flux of solute is now a function of this chemical potential discontinuity [93] and particle dimensions are a linear function of time rather than parabolic, as in diffusion control. For ternary and higher systems the growth rate is controlled by the rate of incorporation of the

slowest element.

2.5.3 Interface Motion Mechanisms

Under both interface and diffusion control, there are two methods by which the interface can advance.

(a) Continuous growth can occur with atoms crossing the interface at all points so that it moves normal to itself as a whole [67,94].

(b) Alternatively atom transfer may only occur at certain points along the interface, e.g. steps on the interface. The ledge will move laterally along the interface, which as a result advances normally (fig. 2.28). Lateral growth has been modelled by Cahn [68], who also gave criteria for this type of growth based on periodic equilibrium lattice configurations. In order to grow by a lateral mode a surface must attain a metastable equilibrium configuration in the presence of the driving force, which is often associated with a sharp and/or a singular surface. The surface remains in this configuration until the passage of a step when it advances through the step height ending in an identical configuration. Normal growth results if metastable equilibrium cannot be attained. The excess free energy per unit area of a step is calculated from:

(a) the increase in free energy in creating unit volume of homogeneous material

(b) the work in placing that volume in an environment of varying composition, order or site fraction, i.e. the gradient energy [95].

The variation of surface tension (σ) with interface position (α) is then obtained (fig. 2.29).

$$\sigma(\alpha)=[1+g(\alpha)]\sigma_0 \qquad \ldots(26)$$

By considering the excess free energy due to a slight inclination from a crystallographic direction for the interface, ε the excess free energy per unit length of step in a diffuse interface is:

$$\varepsilon \approx a\sigma_0(g_{max})^{0.5} \qquad \ldots(27)$$

a=lattice parameter for primitive cubic systems

Cahn's criterion then identified three areas, dependent on driving force ($-\Delta F_V$).

(i)

$$0<-\Delta F_V<\sigma_0 g_{max}/a \qquad \ldots(28)$$

Classical lateral growth by steps which control growth with an energy ε independent of $-\Delta F_V$.

(ii)

$$\sigma_0 g_{max}/a<-\Delta F_V<\pi\sigma_0 g_{max}/a \qquad \ldots(29)$$

Lateral growth has now been modified by critical nucleus size and spiral arm spacing as the latter are now comparable in size to the step width. This regime gives a gradual transition from lateral to uniform advance.

(iii)

$$\pi\sigma_0 g_{max}/a < -\Delta F_V \qquad\qquad .....(30)$$

Normal growth without steps.

These growth rates are extremes and often growth control is a mixture of diffusion and interface, by mechanisms intermediate between local and Para-equilibrium [70-72].

In the case of welding microstructure the compositions and cooling rate seem to give ferrite growth by a ParaE mechanism and rates calculated upon this [8] give excellent agreement with experimental weld measurements [96,97]. The effects of various compositional and process variables, which have been illustrated in the systematic weld series studied by Evans [96,98-102] are consistent with diffusional growth of a grain boundary nucleated phase. The hardenability effects of alloying elements such as Ni, Mn, Cr, Mo, Nb, Ti, V and Zr have been observed in reduction of α due to reduced growth rate at increased alloy levels, although C is most potent in this respect. In addition segregation of elements such as Mo and soluble B to γ grain boundaries causes α to be almost eliminated by removal of nucleation sites.

2.5.4 Widmanstätten Ferrite

The formation of allotriomorphic ferrite involves a reconstruction of the FCC γ lattice into a BCC α lattice, which is effectively simultaneous transformation and recrystallisation so that diffusion parallel to the interface destroys the shear part of the lattice change (fig. 2.30) [78]. High atomic mobility is required, but the absence of significant strain energy reduces the driving force for transformation. As the weld cools after initial α formation, the undercooling increases increasing the driving force, at the same time reducing atomic mobility. This gives rise to a change in transformation product from α to Widmanstätten ferrite, which is also termed aligned ferrite with second phase, emanating from the grain boundaries (primary) or the α/γ interface (secondary). Fast cooling, high alloy content and some grain boundary segregants promote primary Widmanstätten α as the grain boundaries are not saturated with allotriomorphic ferrite, otherwise nucleation occurs at the α/γ interface. The exact nucleation behaviour of this phase is unclear although the temperature at which it becomes thermodynamically possible (W_s) can be predicted accurately [81]. Use of this parameter, however, does not give any effect of cooling rate, which has been observed in welding trials [103]. This is the subject of current research. The phase itself is the product of a displacive transformation which should introduce a large strain energy term, incompatible with its low undercooling below Ae_3 [104]. This term, however, is largely eliminated by the simultaneous formation of two back-to-back plates whose shear displacements cancel to a large extent. The habit planes of these two variants are slightly misoriented, giving rise to the characteristic wedge shape (fig. 2.31). As with α, the growth rate of Widmanstätten α is carbon controlled as the low undercooling necessitates carbon equilibrium at the interface. However, the Widmanstätten α grows more rapidly because multidirectional diffusion occurs from the tip compared with unidirectional diffusion ahead of a plane boundary (fig. 2.32). Use of Trivedi's analysis for diffusion controlled growth of a plate [105,106] allows the growth rate for this phase to be calculated, which, due to the rapid development of Widmanstätten α in welds, can be

treated isothermally.

The values obtained for low alloy MMA weld deposits (Fe, 0.029-0.100 C, 0.55 Si, 1.01-1.15 Mn wt%, 267-342 ppm by wt O) for Widmanstätten α growth rate range from 52 to 552μms^{-1} (slower for higher [C])[6]. The γ grain widths for these deposits were 95 and 121μm respectively meaning that Widmanstätten α plates would cross the grains and impinge on the other side in 0.1 to 0.2 seconds, unless blocked by α_{acic}.

The displacive nature of this product means that the effect of alloying elements such as Mn, Ni and Cr is less than for α, as has been noted by Evans and others, where variations of Widmanstätten α volume fraction with alloy content are generally less than for α. At high alloying levels the Widmanstätten α phase field will be incorporated into the bainite phase field and Widmanstätten α will not form as a distinguishable phase ($W_s = B_s$). Again elements such as Mo which remove grain boundary nucleation sites will reduce the amount of Widmanstätten α formed in a similar way to α. Boron, which has a strong retarding effect upon nucleation of allotriomorphic ferrite has a negligible effect upon displacive products and would not be expected to retard formation of Widmanstätten α.

2.5.5 Acicular Ferrite

Unlike the earlier phases, this does not have a direct analogue in wrought steels and is beneficial to toughness (α and Widmanstätten α allow too much crack development for good toughness). This phase is observed as a fine interlocking network of ferrite plates in the centre of prior γ grains; the interlocking plates provide large numbers of non-parallel grain boundaries to hinder crack propagation especially cleavage cracks [60,107]. The transformation mechanism for this phase has not yet been deduced although suggestions, based on welds quenched to give partial transformation, have been made that it is Widmanstätten α nucleated upon deoxidation products [65]. However, some researchers consider it to be closer to a form of bainite [108], although conclusive proof of this does not exist as yet. In either case the mechanism is a predominantly displacive one, the difference arising from the amount of carbon diffusion associated with the transformation, this being much less for bainite. As a result bainite gives an incomplete reaction, where the transformation stops at the T_0 temperature (see section 2.5.6.2) rather than proceeding to the Ae$_3$ equilibrium. This would raise the amount of associated microphase (likely to be martensite at the low carbon/alloy levels used) and reduce the beneficial effects on toughness.

The strong effect of α_{acic} on resistance to cleavage crack propagation, fig. 2.33, in particular and toughness in general mean that most studies on this phase have been done on an empirical basis with little theory. Often they are related to toughness measurements such as Charpy impact tests and so also include the effects of yield stress (σ_y) not just volume fraction of acicular ferrite.

Acicular ferrite is thought to form after grain boundary allotriomorphic ferrite, before bainite and in competition with Widmanstätten α side plates. Inhibition of allotriomorphic ferrite can be achieved by increasing the hardenability of the weld metal, which suggests that increases in the

strong hardening elements Mn, Ni & Mo would allow greater amount of α_{acic} to form. However, the effect of these elements on side plate and microphase formation must be considered and, considering the importance of inclusions on α_{acic} nucleation, on inclusion composition and distribution. Also individual effects may not be additive with alloying elements altering the individual behaviour when mixed e.g. Mo-Nb and V-Nb combinations [84,109].

2.5.5.1 Manganese

This is one of the major alloying elements, both in wrought and weld metals, as it combines a deoxidising behaviour in the melt with solid solution strengthening and increased hardenability. When used in wrought steels solely for deoxidation the residual Mn content is $\approx$ 0.5wt%, for weld metals this may be raised to nearly 2.0 wt% depending on process and required strength level. Evans [100] studied the effect of Mn in both as-deposited and reheated weld runs, and, subsequently, the effect of cooling rate (heat input) and austenitising temperature on the same weld series were investigated [102]. These indicate that manganese refines weld microstructure and promotes α_{acic} at the expense of grain boundary ferrite [84,98,112]. Increased cooling rates were found to increase the proportion of α_{acic}, so that a lower Mn content would give the same effect. For reaustenitised specimens [110] then the proportion of α_{acic} decreased in the order:

$$\text{As-welded} > T_\gamma = 1350°C > T_\gamma = 1000°C$$

T_γ=reaustenitisation temperature

This is consistent with the effect of Mn, cooling rate and T_γ on hardenability and was reflected in lower γ-α transformation temperatures as all three variables increased. These would all retard formation of allotriomorphic α at the grain boundaries by:

(i) Inhibiting diffusional processes - cooling rate and [Mn].

(ii) Reducing nucleation - T_γ through reduction of grain boundary area and [Mn] through free energy effects, as it is a γ-stabliser.

Evans' results indicate a slight decrease in lath structure (aligned ferrite with second phase) with increased [Mn], which will be due to similar effects as above.

Farrar & Watson [113] calculated matrix Mn content from bulk content, oxygen level and flux type. They assumed an inclusion type (from flux composition) to give a volume fraction of inclusions from which they derived the Mn removed from solution to leave matrix [Mn]. This was plotted against proportion of α_{acic} at [O] levels of <400ppm, 400-500ppm, >500ppm, which show similar curves for the first 2 as data were limited for the third case, fig 2.34. Their suggestion was that [Mn] was the controlling factor in α_{acic} formation through its hardenability effects with a critical value of 1.1wt%. However, no mechanism is presented and the data show wide variations which could mask changes occuring with varying [Mn]. Also, hardenability is not dependent solely on [Mn] and so all alloying should be considered.

21

2.5.5.2 Nickel

Like manganese, nickel has a large effect on hardenability and its effect on the proportion of α_{acic} is similar, in that it promotes α_{acic} at the expense of grain boundary ferrite, although no report of its effect on bainite formation is noted [84,109]. The mode of operation of these elements in this respect is different and so their use together can give element interactions effects. An increase in [Ni] from 2.2 to 2.6wt% gives a slight increase in α_{acic}, the effect increased with T_γ and cooling rate variation gave much less change than for the manganese series. Again transformation temperatures decreased as alloy content increased, in 0.09 C-1.5 Mn wt%, the addition of 2wt% Ni caused a decrease of 50- 120°C in the γ-α transformation start temperature $(T_s^{\gamma-\alpha})$ depending on cooling rate [99], so retarding proeutectoid ferrite and allowing more transformation to α_{acic} once nucleated. The same hardenability effects of variation in optimum toughness alloying levels with heat input [84] were observed as were toughness decreases due to martensite/bainite formation [112] and increases in σ_y, at high levels of Ni (>3wt%). However, at higher Ni contents the microphases will be replaced by an increased amount of retained γ, so causing an increase in toughness [109]. Ni also raises the stacking fault energy of α and so reduces the three dimensional dissociation of dislocations, which allows more stress relaxation by plastic deformation and is an inherent toughening property of Ni.

2.5.5.3 Molybdenum

Mo has a very strong hardenability effect for low alloy steels which will reduce proeutectoid α content and sideplate formation; also it causes a deep bay in the TTT curve above the bainite transformation, depressing the bainite start temperature (B_s). Therefore, it should be very powerful in promoting α_{acic} as it inhibits both grain boundary ferrite and bainite and this has been found to be the case [109,114], where the presence of Mo increased the α_{acic} content. Levels of Mo up to 1.1wt% have been studied in combination with Mn levels of 0.6, 1.0, 1.4 and 1.8wt% [100] and constant [C], although there was a slight increase in [C] with increased [Mo], an effect also noted with Mn. Up to 0.5wt% Mo increased the proportion of α_{acic} at the expense of allotriomorphic α, which is eliminated at 1.1wt% Mo, when α_{acic} was being replaced by aligned ferrite with second phase, decreasing toughness. Increased [Mo] was associated with a decrease in α_{acic} lath size, but an increase in colony size for aligned ferrite. Its effect on toughness, especially in reheated structures, is not so dramatic due to Mo_2C clustering/precipitation which causes the yield stress to increase. These have been suggested as grain boundary pinners [5] and reports of decreasing γ grain size with increasing [Mo] exist [109]. In reheated HSLA welds the presence of Mo and Mo_2C may be responsible for increased Nb(C,N) precipitation [116]. Molybdenum segregates to prior γ grain boundaries, where its affinity for carbon will cause clustering and reduced mobility of the latter species. This will retard the formation of ferrite in grain boundary regions to lower temperatures, as a greater driving force is required at higher carbon levels to overcome the clustering effects. Acicular ferrite, being an intragranular phase, will be less affected leading to an increase in its volume fraction. Mo will also depress the bainite start

temperature (B_s) as the driving force for nucleation is reduced, again by carbon clustering at the grain boundaries and by partition of carbon from α_{acic} intragranularly nucleated. Garland and Kirkwood [109] also reported an effect upon the microphase content with increased Mo giving a more even distribution of fine islands of high C twin martensite, which improves cleavage crack resistance as the crack length that grows initially in α' is reduced.

These three elements will have an optimum level for toughness due to a balance of:

(i) Promotion of α_{acic} through hardenability effects up to 90% (beneficial).

(ii) Increase in yield strength due to solid solution strengthening or precipitation (detrimental).

(iii) Excessive hardenability leading to formation of areas of martensite or total removal of grain boundary ferrite, which may lead to 'tramp' elements embrittling the grain boundary (detrimental).

Their general behaviour is shown in fig. 2.35. Abson and Pargeter noted a variation of alloy effect with flux due to:

(a) variations in inclusion type and content,

(b) variations in total alloy content.

2.5.5.4 Silicon

This is another common element found in weld deposits due to the large amounts of SiO_2 and silicates used as flux constituents. In addition to inclusion effects which inevitably decrease [O] as [Si] increases, the effect of [Si] from 0.2 to 0.9wt% was studied by Evans [99] using his systematic C-Mn weld series. At low [Mn] (0.6wt%) increasing Si promoted α_{acic} at the expense of allotriomorphic α and Widmanstätten α, but at higher [Mn] (1.4wt%) there was an increase in microphase content (M/A as the presence of Si inhibits carbide formation), although the volume fraction of α_{acic} remained reasonably constant at $\approx$ 75%. No study of the changes in inclusion content associated with these microstructural variations was presented.

2.5.5.5 Chromium

This has been relatively little studied in low alloy (i.e. non-stainless) steel deposits, but varying [Cr] in submerged arc HSLA welds [121] indicated that [Cr] above 0.5-1.0wt% caused a decrease in the percentage of α_{acic}. Use of Ti/B fluxes was found to maintain the proportion of α_{acic} ($\approx$ 80-90%) up to 0.7wt% Cr. The general effect of Cr was an increase in hardenability so that the proportion of allotriomorphic α decreased and the amount of bainite and M-A microphase increased. Similar results were noted for electroslag welding of 0.18 C-1.1 Mn-0.4 Si wt% steel with different filler wires varying [Cr], [Mo] and [Ni] [122], where a continuous decrease in allotriomorphic α was noted. Initially this was replaced by α_{acic}, but above 0.5wt% Cr, 0.2wt%Mo this was rapidly replaced by bainite causing a decrease in toughness.

Neither study undertook an analysis of the inclusion population although Snieder & Kerr noted no variation optically, which would be expected from the presence of Al, Si and Ti in the flux (all stronger oxide formers). The formation of chromium carbides may give rise to grain boundary

pinning [111], but no direct evidence of this has been cited.

2.5.5.6 Aluminium

As with Si and Ti, this element will have a large effect on the inclusion population, which will probably outweigh any solid solution effect, although Al tends to reduce hardenability. Dilution of Al from baseplates [123] caused a change in microstructure from α_{acic} to ferrite with aligned second phase, probably bainite laths as the changes in hardenability would have been insufficient to cause formation of Widmanstätten α. This change is most likely due to a removal of nucleation sites for α_{acic} promoting grain boundary or α/γ interface nucleated phases. The strong affinity of Al for O and the large presence of the latter in the weld pool causes the chief effects of Al to be related to the inclusion population. Here, it tends to reduce the O available for formation of titanium oxides [124-126] and causes a decrease in the nucleation behaviour.

2.5.5.7 Titanium

Titanium in solid solution will cause an increase in hardenability and an optimum level of $\approx 0.05wt\%$ [84] exists for promotion of α_{acic}. However, this optimum cannot be explained by hardenability arguments alone [116], as the range of [Ti] over which α_{acic} is promoted does not vary with variation of total hardenability (achieved through different Mo levels). This suggests that Ti exerts a strong influence on the nucleating inclusion population. Ti also improves toughness by removing N from solid solution and so reduces solid solution strengthening.

Excessive Ti levels ($\approx 0.2wt\%$) cause a large increase in hardenability and the formation of bainitic structures in preference to α_{acic}. In addition inclusions become Ti rich and more angular [116].

2.5.5.8 Boron

If retained in solid solution, achieved by tying O and N up with Al and Ti additions, then B segregates to prior γ austenite grain boundaries, where it prevents grain boundary nucleation of ferrite [127,128]. Elimination of allotriomorphic α then leads to an increase in α_{acic} [84,109,129], although if the weld is too heavily alloyed martensite and bainite predominate. Boron has a low solid solution hardening effect and so is preferable to Ni, Mn and Mo as an element to increase in hardenability. Continuous cooling transformation (CCT) curves on reheated Ti-B fluxed weld metals [130] reveal a large decrease in the transformation temperature for allotriomorphic α, but not with α_{acic}, consistent with it being a displacive product (Widmanstätten α or α_b).

2.5.5.9 Microalloying Elements-Niobium and Vanadium

These elements are not generally added deliberately, but are often diluted into a weld pool during welding of HSLA steel base plates, particularly line pipes where up to 60% dilution can occur.

Nb causes large increases in the hardenability of steels [131] and, at low levels of α_{acic} (50-80%), can cause an increase in the proportion of α_{acic}. However, segregation of Nb to

24

solidification boundaries causes excess hardenability there and the formation of isolated lath α' [84]. This, along with increases in σ_y due to Nb(C,N) precipitation cause the beneficial effect of increased α_{acic} on toughness to be negated. The low solubility of NbC causes it to be precipitated, during cooling, on prior γ grain boundaries and it can give grain boundary pinning as in the thermomechanical processing of HSLA alloys, although in welding there is no continuous deformation and break up of γ grains. The presence of NbC at prior γ grain boundaries will modify grain boundary nucleation and inhibit allotriomorphic α; the bainite reaction may not be affected as most NbC precipitates in γ at prior γ grain boundaries leaving the α/γ interface unaffected. By contrast, vanadium carbides precipitate mainly at the α/γ interface [132,133] and so would be expected to affect the formation of bainite more. This is found to be the case both in wrought steels [134] where the behaviour of V is similar to that of Mo and in welds [84]. In the latter case a variable effect on toughness is found; at low heat inputs [135] 0.05-0.1wt% V was beneficial causing an increase in α_{acic} at the expense of upper bainite. The optimum level of V depended on the Ti content of the weld metal. At higher heat inputs [136] the reduced cooling rate gave a decrease in toughness with increased [V]. The maximum proportion of α_{acic} achievable through variation in [V] was $\approx 80\%$; this was also achieved by the addition of 0.09wt% V to a 0.03wt%Nb HSLA weld deposit [129]. This combination is thought to be more beneficial than the sum of the individual effects as both allotriomorphic α and α_b are inhibited. However, use of these elements is limited due to increases in σ_y brought about through carbonitride precipitation.

It may also be that V changes the potency of inclusions for nucleation of α_{acic} as the change in hardenability for 0.09wt% V is not great but %α_{acic} increased from 25 to 84 at the expense of grain boundary nucleated lath structures. This may also account for the dependence of optimum [V] on [Ti].

2.5.5.10 Rare Earth Metals

Pacey et al. [116] showed that in welds containing a high level of α_{acic} an increase in [Zr] from 0.002 to 0.029wt% caused an increase in lath structure from 5 to 17% with a small decrease in toughness. Initial small increases in Zr content caused a small increase in the proportion of α_{acic}.

Rare earth metal additions eg 0.15-0.20wt% Ce and 0.04-0.10wt% Y, in combination with rutile coatings [137] give rise to large increases in toughness. In addition hydrogen induced cracking was reduced by the use of Ca, Ba, Se and Te, although rare earth metal additions greater than 0.1wt% impaired toughness for unspecified reasons [112].

Various patents use Mg in coatings to achieve higher basicity [138] or to reduce TiO_2 [139] to Ti, active in the weldpool. These improvements may cause a variation in inclusion content but not change weld metal microstructure. Improved toughness with high [Zr] contents (1wt%) is associated with removal of N rather than with increase in α_{acic}. Poor toughness with excess [Mg] is ascribed to increases in both σ_y and microphase content.

25

In the case of cerium, removal of sulphur may be important and most rare earth metal (REM) effects can be explained through variation in inclusion content [140]. REM and Ca have similar effects on grain size - a refinement - and inclusions [137].

One major effect of these deoxidants is to reduce TiO_2 to titanium which acts as a deoxidant in the weld pool. No indication is given if they act as grain refiners.

2.5.5.11 Tramp Elements, Sulphur and Phosphorus

Toughness studies have concentrated on the segregation of these to grain boundaries causing embrittlement through reduction in Fe-Fe bond strength or sulphide distribution, as weak interface strength gives ready voiding and crack nucleation, often causing lamellar tearing. The effect of [S] from 0.007-0.046wt% was studied by Evans [101] in Fe, 0.06wt% C, 1.38-1.41wt% Mn, 0.037wt% Si weld metal and, in the same series, [P] from 0.007-0.040wt%. Increasing sulphur caused an increase in the oxygen content (from 437 to 516 ppm), but there was little variation with [P]. Phosphorus content did not have any noticable effect upon the as-deposited microstructure, but there was a decrease in α_{acic} proportion from 75 to 63% with increase in [S] in a somewhat stepped function. This change was not due to any effect of S in solid solution through free energy or nucleation site changes, but instead centred on the inclusion population. Analysis of $\approx$ 20 inclusions revealed the presence of an FCC surface layer (a=0.42nm), probably TiX, in the low sulphur welds, which was replaced by a MnS type surface layer with small TiO/MnO spinel particles at higher [S]. Both types of surface layer showed a tendency to detach. The low sulphur solubility and large number of preexisting oxide particles mean that its effects are associated with the latter and not the solid solution.

2.5.5.12 Carbon

The interstitial, and highly mobile, nature of carbon in steels exerts a profound influence over phase transformations in steels, carbon being the most effective γ stabiliser. In weld metals, the effects of [C] have been studied by Evans [96], Dolby [84] and Garland & Kirkwood [109], all of whom related it to the toughness of the final weld metal. With its large effect on hardenability, it is expected that increasing carbon would reduce the amount of allotriomorphic ferrite by depressing transformation temperatures and, more importantly, by reducing growth rates. This was found to be the case with α_{acic} increased at the expense of grain boundary ferritic phases. In addition, there was an increase in carbide precipitation, on reheating, and an increased tendency to form high carbon martensitic phases in the microphases, both of which would reduce toughness. Evans also noted a change in the apparent aspect ratio for α_{acic} laths, the reason for which is unclear, but may be due to alteration of carbon diffusion rates or lattice parameters so that growth rate or habit plane vary. Without detailed transformation theory this must remain speculation. In general, there is an optimum value of [C] for toughness (0.07-0.09wt%) to ensure adequate hardenability, without excessive carbide formation or strength.

2.5.5.13 Cooling Rate / Heat Input

The general effect of alloying elements is that increased hardenability, i.e shift of the diffusional C curve to the right, and inhibition of the bainite reaction, enhance α_{acic} formation. This is also reflected in the effect of cooling rate on α_{acic} - a fast cooling rate (low heat input) corresponding to a higher hardenability. Therefore, at slower cooling rates, a higher hardenability, i.e. a larger alloy content, is required to shift the proeutectoid curve further to the right.

This introduces a further problem, in that, alloying elements may have opposite effects on toughness at different cooling rates, as noted by Dolby [84].

Stress relief does not affect the proportion of α_{acic}, but may bring out its benefits by tempering lath martensite, although any precipitation will reduce toughness by raising the yield stress.

2.5.6 Microphases

This is a general term covering all the final constituents to form and, as such, includes martensite, retained austenite, carbides and bainite, although considerable confusion exists as to which phases are which, bainite or martensite. All these phases are present in wrought steels and have been extensively studied with the deduction of much of the governing thermodynamics and kinetics. In welding they arise from:

(a) Overalloying - excessive hardenability so that insufficient time is available to form the previous ferritic phases resulting in α_b or α' formation. In the case of large amounts of γ stabilisers, then γ will be retained down to room temperature.

(b) Low heat input - this corresponds to fast cooling and has the same effect as excessive hardenability with higher cooling rates leading to the presence of more α_b or α' .

(c) Insufficient nucleation sites - if the inclusion distribution is not large enough or of an incorrect type, then nucleation of α_{acic} cannot occur, leaving more γ available for transformation to α_b or α'.

The volume fraction of Widmanstätten α and α_{acic} do not concentrate solely on the ferritic plates but also include the associated microphase which will be a function of the volume fraction transformed and hence the extent of carbon partition into the remaining untransformed γ. The extent of diffusion and temperature of each of these phases will determine the extent of homogenisation of any carbon partition. The carbon enrichment will lead to a variation in B_s and M_s and hence the distance from the interface at which each phase forms will be determined by the rate of redistribution of C in γ ahead of the γ/α interface. This hypothesis still requires experimental verification.

The inclusion of microphase regions into the volume fraction of Widmanstätten α and α_{acic} means that its variation in these regions with alloy content is not generally reported and in fact its variation within the total volume fraction of that phase is not considered, although it may exert a profound influence over the mechanical properties of that phase, as a whole. More commonly the reports on microphase content refer to islands of M-A-C within the as-deposited

microstructure. The difficulty of further defining which phase is present, without the use of TEM, leads to the use of the covering 'microphase' label.

2.5.6.1 Theory of Bainite Formation

Bainite, like Widmanstätten α, is the product of a displacive reaction [141-144], but involves substantially less carbon diffusion and is seen in steels to grow in a 'sheaf' formation. Close examination of a bainite sheaf reveals a substructure of ferrite sub-units, which are lenticular in shape. These sub-units form in an initial 'shear' transformation from FCC to BCC lattices so that initially α_b forms with the same composition as the parent austenite. This mechanism involves an invariant plane strain (IPS, related to the Bain strain) and introduces the surface relief, habit plane and orientation relationship observed for this phase; the condition of minimisation of strain energy results in the lenticular morphology adopted by the sub-units. As a result of the shear transformation the ferrite formed is supersaturated with respect to carbon driving post shear diffusion of this species into the surrounding γ. This means that the next sub-unit to form will do so from γ enriched in C and so under a reduced driving force (fig. 2.36). The situation is soon reached where the C enrichment of γ causes both BCC and FCC structures to have the same free energy and so further shear formation of α from γ is thermodynamically impossible. The variation of the carbon level at which γ and α of the same composition have the same free energy with temperature defines the T_0 curve. Formation of bainite then ceases and an incomplete reaction is exhibited, stopping at T_0 (or more often T_0' which includes the effect of the strain energy involved, $\approx 400 Jmol^{-1}$), rather than at the equilibrium Ae_3. On further cooling the untransformed γ can be retained down to room temperature or can precipitate carbides between the lenticular sub-units. This is upper bainite; at lower temperatures, less carbon diffusion can take place and so Fe_3C tends to be precipitated within the sub-units themselves. These carbides precipitate in one variant of the Pitsch orientation [141,145] within a sub-unit, in contrast to the 3 in an autotempered martensite, often at 60° to the length of the sub-unit (fig. 2.37). The single variant arises from the need to minimise strain energy.

2.5.6.2 Martensite Formation

This is another displacive reaction product, but, unlike bainite, retains carbon in solid solution and so is very hard and brittle as C in solid solution pins dislocations very effectively. The transformation mechanism, involving two IPS's to accomplish lattice and shape changes is well known [94] and the theory for diffusionless transformations was first deduced from this phase. The total absence of diffusion during formation of this phase means that there is generally no increase in volume fraction with time at temperature, once initial (rapid) formation of α' has occurred. Instead the volume fraction is determined by temperature as this determines the driving force available for transformation. The IPS nature of the transformation involves a large strain energy and this will increase as the volume fraction of α' increases. It is this strain energy that dissipates the driving force so that only a certain volume fraction can form at any particular

temperature and increased volume fraction is only achieved by further reducing temperature. An expression for the volume fraction of martensite (f_{ms}) as a function of undercooling below M_s (ΔT) has been empirically determined:

$$(1 - f_{ms}) = \exp(-0.011\ \Delta T) \qquad \qquad .....(31)$$

Martensite is a metastable phase, which is kinetically preferred, so that on reheating diffusion of carbon will occur to precipitate as fine carbides and leave ferrite.

2.6 Modelling of Welding Processes

The technological importance of welding means there are great incentives in being able to model and predict the properties and performance of these joints. However, it is only recently that sufficient data and theory have been obtained, along with access to computing facilities, to enable such a program to be undertaken. The main areas of interest will be briefly reviewed here.

2.6.1 Heat and Fluid Flow

The flow processes in a weld pool and baseplate are important in determining the extent of the HAZ, solidification times (and subsequent cooling in the solid state), weld pool shape, solidification substructure and degree of segregation. Heat flow problems can be tackled either through closed forms of the governing partial differential equations or by use of finite element methods.

Rosenthal [146-148] initially applied the conditions of a moving point source to derive equations covering heat flow in arc welding. These solutions are still valid for simple geometries and have been used as a basis for more elaborate, if less successful, formulations, taking into account factors such as temperature dependence of thermal properties [149], surface heat losses [150], latent heat [151] and finite size of heat source [152]. Despite the assumptions, solutions based upon Rosenthal's equations give good agreement for weld pool shape and HAZ (where assumptions of purely conductive heat transfer are more valid) isotherms, especially in welding of thin sheet, where heat flow is largely two dimensional.

In arc welding processes the weld pool may undergo convective motion driven by
- electromagnetic
- buoyancy and
- surface tension forces,

and these can be dealt with analytically through the conservation equations [153].

$$\underline{\nabla}.\underline{u} \qquad \qquad \text{(continuity)} \qquad \qquad .....(32)$$

$$\rho\underline{u}.\underline{\nabla}\underline{u} = -\underline{\nabla}p - \underline{\nabla}\mu\delta\underline{u} + \rho g + \underline{J_e}\text{X}\underline{B} \quad \text{(motion)} \qquad .....(33)$$

$$\underline{u}.\underline{\nabla}\rho\ C_p T = \underline{\nabla}k\ \underline{\nabla}T \qquad \text{(thermal energy balance)} \qquad .....(34)$$

ρ=density

$\underline{J_e}$=current density

u=velocity of fluid flow

C_p=heat capacity of fluid

These also describe the arc characteristics and give good agreement (fig. 2.38) as this is effectively steady state. However, movement of the weld pool removes axial symmetry and the 3D solutions [154,155] only give good agreement at very low travel speeds.

The second approach, a full three dimensional approach through finite element analysis can give agreement for more complex welding situations than are covered by Rosenthal. This approach, however, is very costly in both time and computing resources and is not viable for simpler cases covered by the analytical solutions. Economics dictate the use of a coarse mesh in the HAZ, but for accuracy in plotting isotherms increasingly finer meshes are used closer to the arc [156,157], fig. 2.39. This method can be extended to cover residual stresses induced by cooling in welds [158].

2.6.2 Microstructure and Properties

Fewer models have been proposed for these areas although several exist for HAZ hardness and two are well advanced for the weld metal itself:

2.6.2.1 Central Electricity Generating Board (CEGB) Model

Work by Alberry and Clark [159-162], based on Rosenthal equations have modelled grain growth in reheated and as-deposited MMA welds, with applications to repair welds in Cr-Mo steels. This approach has given good results for weld bead dimensions and reheated zone size but does not predict microstructure and is empirical in its approach.

2.6.2.2 Bhadeshia-Svensson-Gretoft (BSG) Model

This [8] is a model developed to predict the volume fractions of

- allotriomorphic ferrite
- Widmanstätten α sideplates
- α_{acic}
- microphases

in low alloy welds, using phase transformation theory outlined above. The major features of this model are, (fig. 2.19, 2.40):

(i) Austenite grain structure is assumed to consist of space filling hexagonal prisms, which is an approximation as it neglects curvature due to variation in heat flow direction. The use of a large (16,000) number of intercept measurements on an image analyser, minimises the error present in γ grain size.

(ii) The TTT curve is predicted using a program [81] based on a modification of Russell's nucleation work [163,164] and takes into account the effects of C, Mn, Si, Ni, Cr, Mo and V subject to the conditions of low alloy content ($\leq$5.0wt% total) and all alloying elements in solid solution. This has been modified to take account of segregation of alloying elements during solidification

30

(assumed to be equilibrium).

(iii) Nucleation of grain boundary ferrite is generally so rapid that further growth can be modelled on the one-dimensional advance of the planar γ/α interface.[†] Because of the high cooling rates and low alloy content growth is assumed to occur under paraequilibrium conditions. The thickening of the allotriomorphs is described by

$$q = \alpha_1 t^{0.5}$$ .....(35)

q = allotriomorphic thickness at time t

α_1 = parabolic rate constant

t = time

The volume fraction of grain boundary ferrite is calculated from the γ grain size assuming growth occurs from $T_s^{\gamma-\alpha}$ ($\gamma-\alpha$ transformation start temperature) to T_1 (first formation of Widmanstätten α i.e. at the intersection of the two C curves on the TTT diagram fig. 2.43). In comparison with experimental welds, α_1, is found to correlate well, but the predicted volume fraction of grain boundary ferrite was approximately half that actually observed. This would indicate an incorrect assumption of growth time; at present, the theoretical volume fraction is modified by the following linear regression equation.

$$V_\alpha = 2.04(\text{calc } V_\alpha) + 0.035$$ .....(36)

This relationship has a 0.97 correlation coefficient, so that the analysis explains $\approx$ 95% of the variation in grain boundary ferrite proportion.

(iv) The volume fraction of Widmanstätten α is predicted considering nucleation at γ/α interfaces, of which only a certain area fraction can nucleate. The subsequent growth rate is then high enough for Widmanstätten α formation to be treated isothermally, based upon a growth rate derived from the work of Trivedi [105,106,166]. Impingement can occur with intragranularly nucleated α_{acic} or with allotriomorphic ferrite on the opposite side of the grain. This is tackled by comparing the time to cross the austenite grain (t_3) with a critical time (t_c), when α_{acic} impingement becomes important. t_c was evaluated from a weld in which impingement had just occurred and was considered to be constant for the whole series; this gives good agreement but is a little weak, needing more theory to back it.

(v) Microphases are considered to be martensite and the maximum volume fraction is obtained from the untransformed γ at the martensite start temperature. Use of the lever rule, assuming maximum α, Widmanstätten α and α_{acic} growth, on Ae_1 and Ae_3' at M_s gives untransformed γ and this gives a reasonable value of microphase content.

(vi) Because of the lack of theory for α_{acic} formation, this volume fraction is estimated by difference, subtracting the volume fractions in (iii), (iv) and (v) from 1. However, good agreement is found for α_{acic} volume fractions.

[†] This has been modified to account for initial nucleation and allotriomorph growth before impingement, fig. 2.41 [166], when decoration of γ grain boundaries, fig. 2.42, occurs.

(vii) The limitations of the model can be summarised as:

(a) theoretical calculations underestimate the proportion of grain boundary ferrite by a factor of ≈ 2.

(b) there is no theory for α_{acic} formation and the volume fraction must be obtained by difference.

(c) there is no prediction of γ grain size.

(d) no prediction of cooling curve is included.

(e) although it takes account of C-Mn-Si-Ni-Cr-Mo and V alloying additions the theory is limited to low alloy steels with elements in solid solution.

Table II.1. Comparison of ingot and weld solidificaton.

	Ingot	Weld
Nucleation and growth	Chill, columnar and equiaxed Hence nucleation	No nucleation just epitaxial growth.
Heat flow	Heat transfer and/or thermal conductivity	No interface resistance, as no mould material
Solidification rate	Range from slow to fast	Generally fast, leads to high thermal gradients and stresses
Solid/liquid interface and shape	Progressively changes with time Planar, cellular, dendritic	Constant pool shape, interface moving continuously
Turbulence	Slight, depending on pouring	Strong, driven by stirring, electromagnetic and Lorentz forces
Composition	Fixed by melt	Adjustable by filler wire/flux

Table II.2. Microstructural classification schemes

Author	Constituent	Previous Description
Widgery	(i) Proeutectoid Ferrite (ii) Lamellar Component (iii) Acicular Ferrite (iv) Others	
Cochrane	(i) Allotriomorphic Ferrite (ii) Primary and Secondary Ferrite Sideplates (iii) Intragranular Ferrite Sideplates	
Abson & Dolby	(i) Grain Boundary Ferrite (ii) Polygonal Ferrite (iii) Acicular Ferrite (iv) Ferrite with Aligned Martensite-Austenite-Carbide (MAC) (v) Ferrite-Carbide Aggregate (vi) Martensite	Proeutectoid Ferrite, Ferrite Veins, Blocky Ferrite, Polygonal Ferrite Ferrite Islands Ferrite Sideplates, Upper Bainite, Lamellar Component, Feathery Bainite Pearlite, Ferrite + Interphase Carbide

Table II.3. Relationships between fractional composition, f_i, and growth rate constant, η.

Morphology	$f^k(\eta_i)$	Asymptotic Values	
		$\eta_i \gg 1$	$\eta_i \ll 1$
Planar	$\dfrac{\sigma qt\pi\eta_i}{2}\exp\left(\dfrac{\eta^2_i}{4}\right)erfc(\eta_i/2)$	$1-\dfrac{2}{\eta^2_i}$	$\dfrac{\sigma qt\pi\eta_i}{2}$
Cylindrical	$\dfrac{\eta^2_i}{4}\exp(\eta^2_i/4)E_1(\eta^2_i/4)$	$1-(4/\eta^2_i)$	—
Spherical	$\eta^2_i\left[1-\dfrac{\sigma qt\pi\eta_i}{2}\exp\left(\dfrac{\eta^2_i}{4}\right)erfc\left(\dfrac{\eta_i}{2}\right)\right]$	$1-(6/\eta^2_i)$	$\eta^2_i/4$

35

Figure 2.1. Schematic representation of flux coated electrode MMA welding processes.
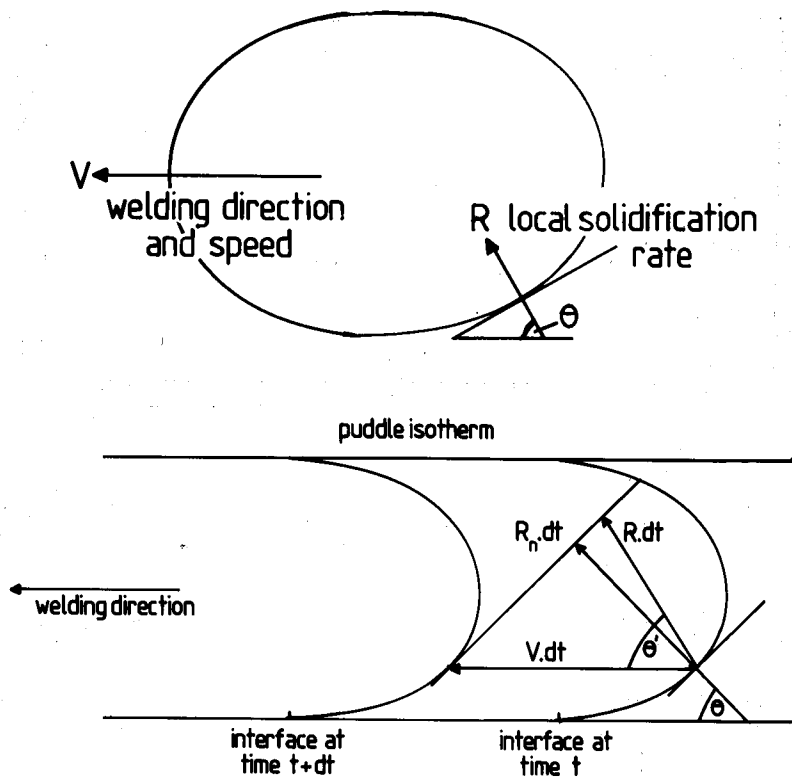
Figure 2.2. Relationship between local solidification rate and welding direction and, (b), considering fast crystallographic growth directions.
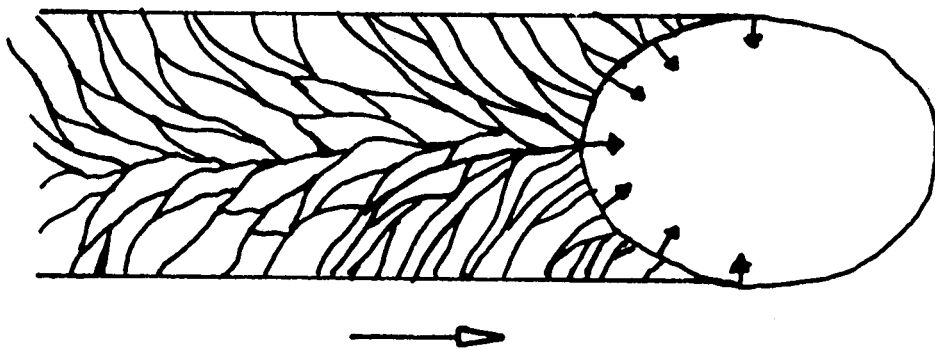
Figure 2.3(a). Elliptical weld pool, slower welding speeds. More progressive direction change in maximum thermal gradient leads to survival of many grains, which are curved, to weld centre.
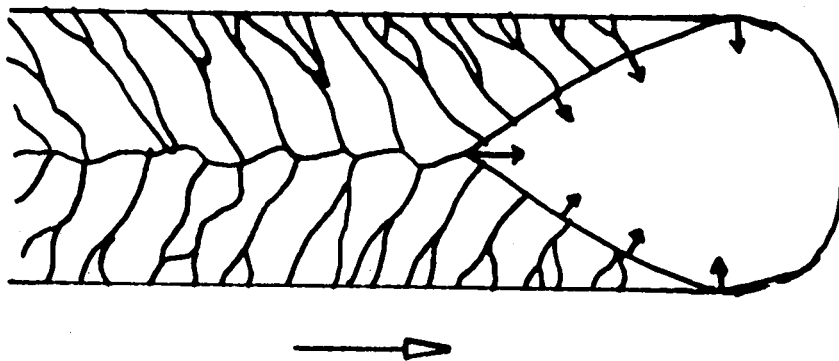
Figure 2.3(b). Tear-shaped weld pool, higher welding speeds. Direction of maximum thermal gradient almost invariant, so that fewer grains survive to weld centre, as competitive growth can occur.
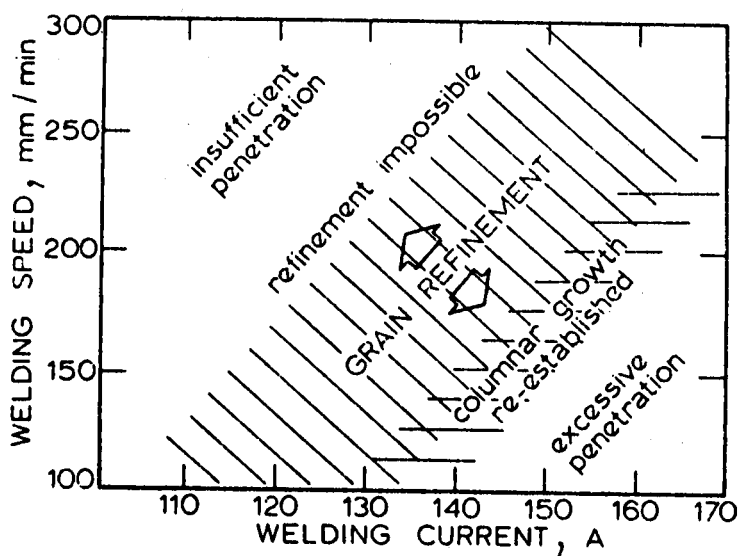
Figure 2.4. Welding conditions giving rise to solidification grain size refinement[9].

composition

solid

C_0/k_0

$C_L = C_0 [1 + \dfrac{(1-k_0)}{k_0} \exp(\dfrac{-Rx}{D})]$

C_0

liquid

0

distance, x

temperature

$T_m - mC_0$

$T_L = T_i + mC_0 \dfrac{(1-k_0)}{k_0} [1 - \exp(\dfrac{-Rx}{D})]$

T_i

temperature

high $\dfrac{G}{R}$ planar   cellular   low $\dfrac{G}{R}$

dendritic

supercooled liquid

λ_1

λ_2

interface
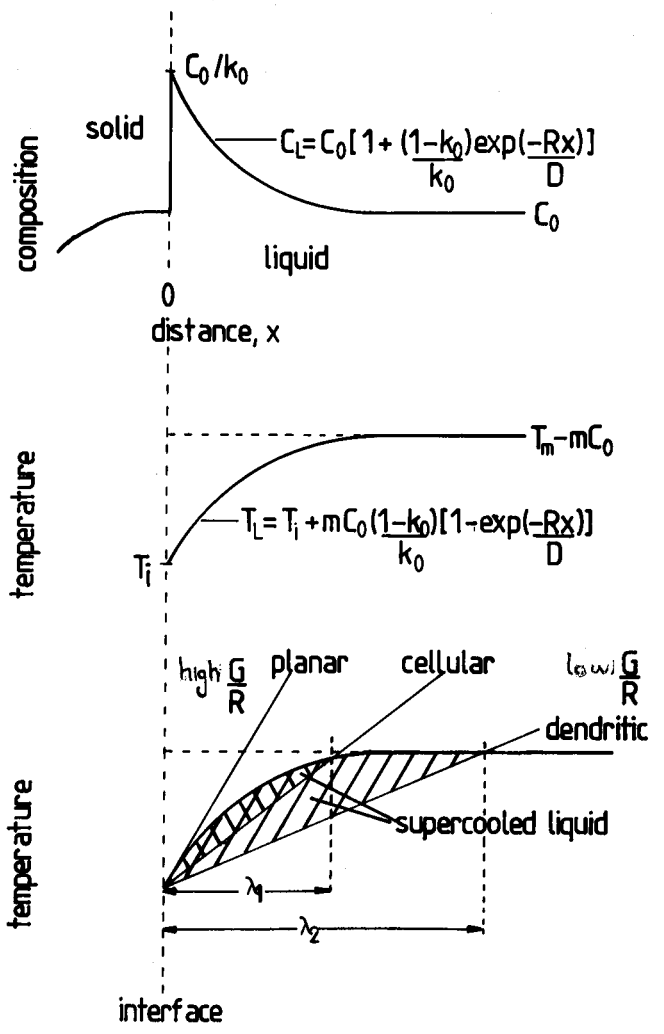
Figure 2.5. Constitutional supercooling.

temperature

T_m

C_0

$k_0 = \dfrac{C_S}{C_L}$

liquid

$C_0 k_0$

C_S C_L slope = m

C_0/k_0
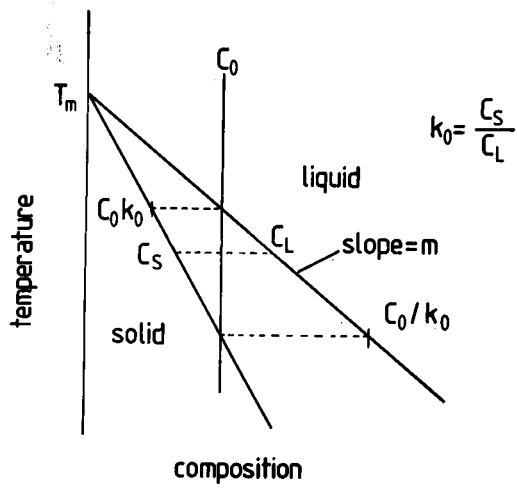
solid

composition

Figure 2.6. Schematic phase diagram.

38

planar growth   cellular growth   dendritic growth
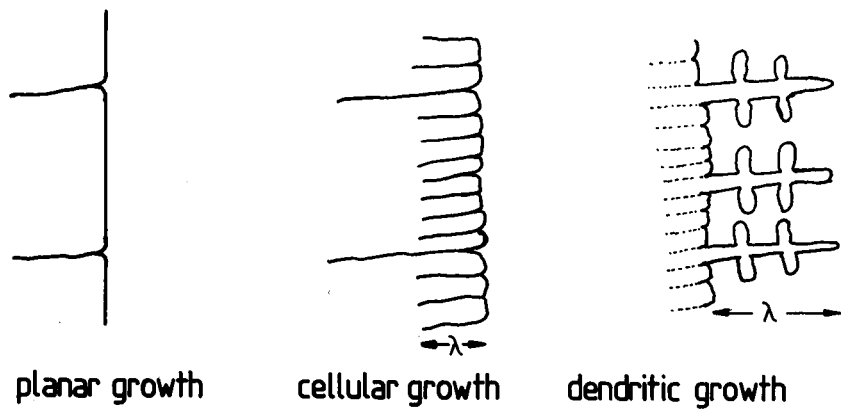
Figure 2.7. Solidification substructures.

(a) Cellular   cross section   (b) Cellular–Dendritic   cross section
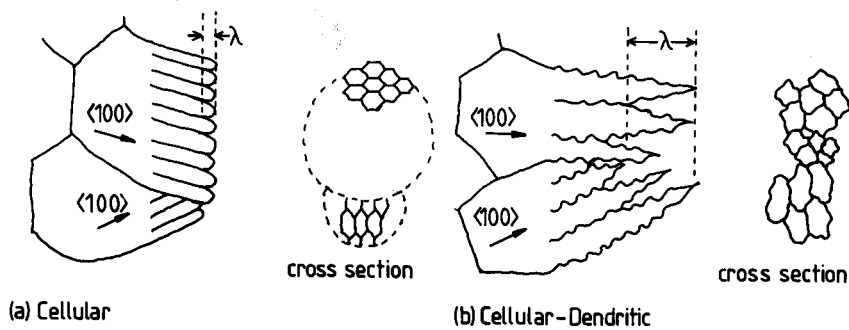
Figure 2.8. Variations in solidification cell characteristics.

low alloy base material

grain growth zone
transition line
planar
cellular
cellular-dendritic
dendritic
cellular-dendritic
cellular
planar
grain growth zone

low R, high T_L
high R, low T_L

high alloy base material
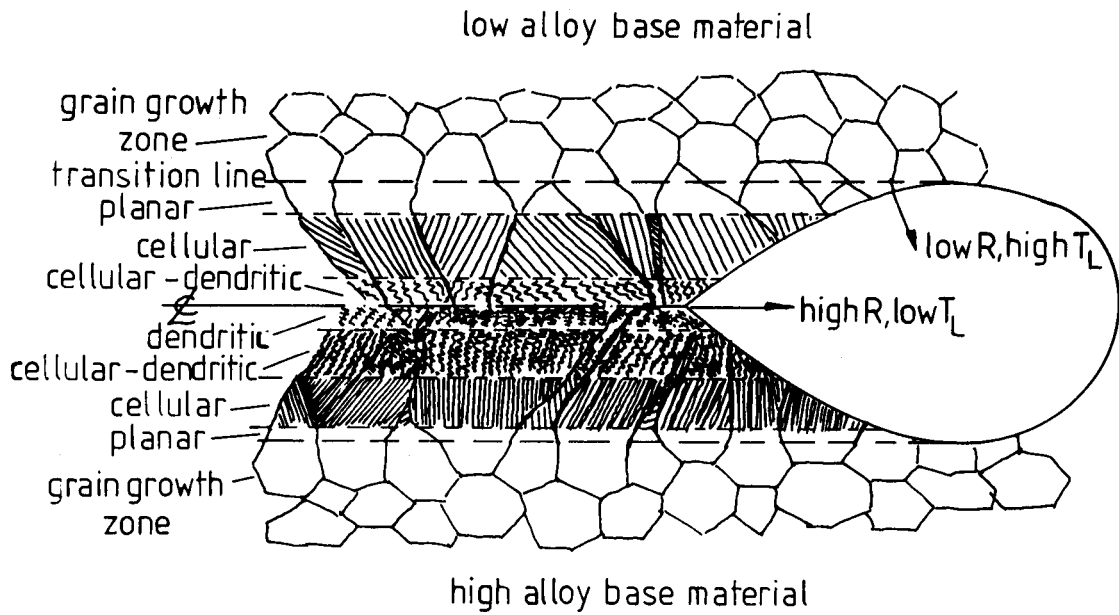
Figure 2.9. The effects of baseplate composition on solidification structures[5].

cell boundaries → growth direction

grain boundary

solute accumulation
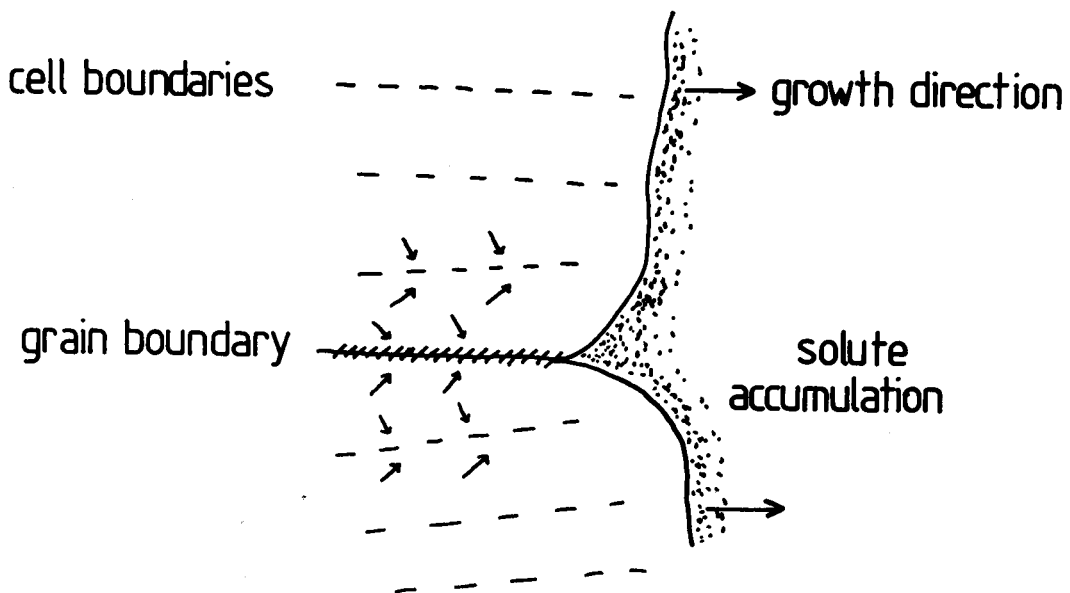
Figure 2.10. Solute segregation to solidification boundaries.
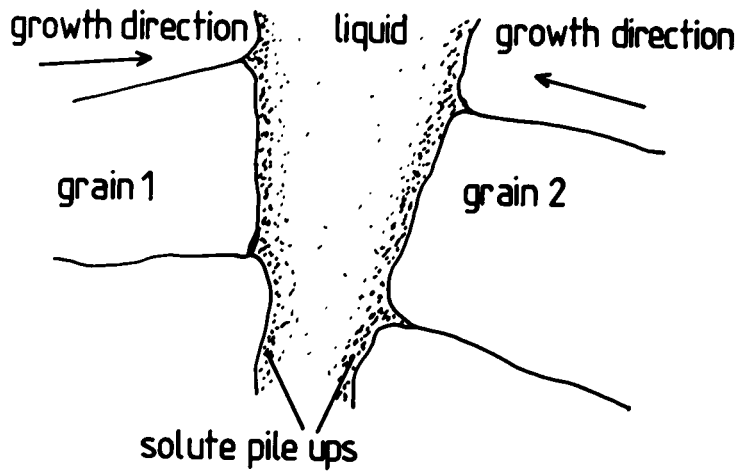
Figure 2.11. Solute trapping by centreline impingement of advancing solid.
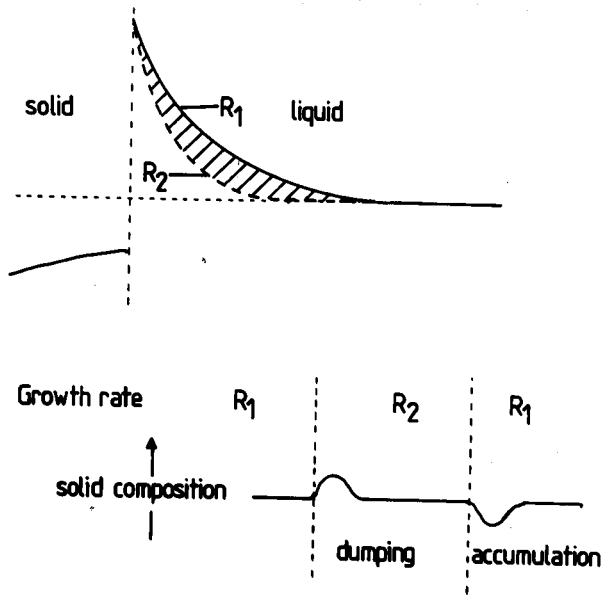
Figure 2.12. Solute dumping and accumulation due to growth rate variations.

41
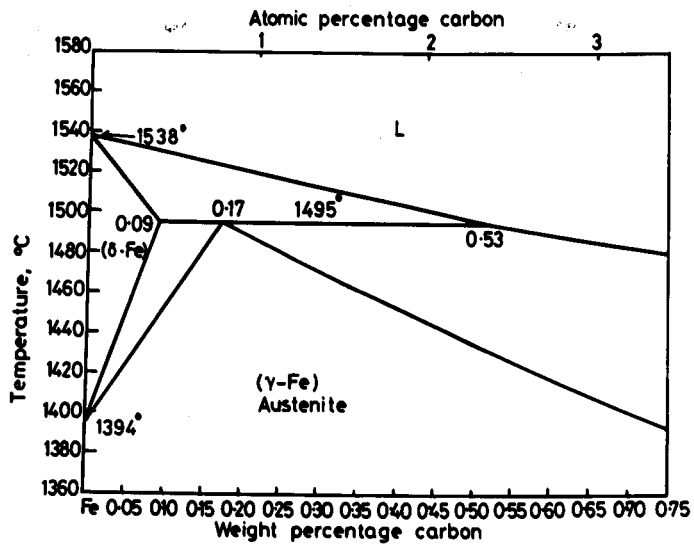
Figure 2.13. Fe-C phase diagram.
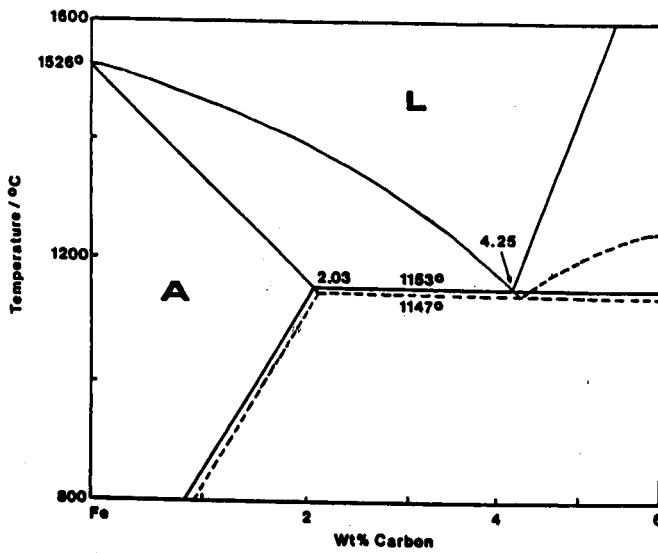
Figure 2.14. Variation of initial solidification phase with cooling rate.
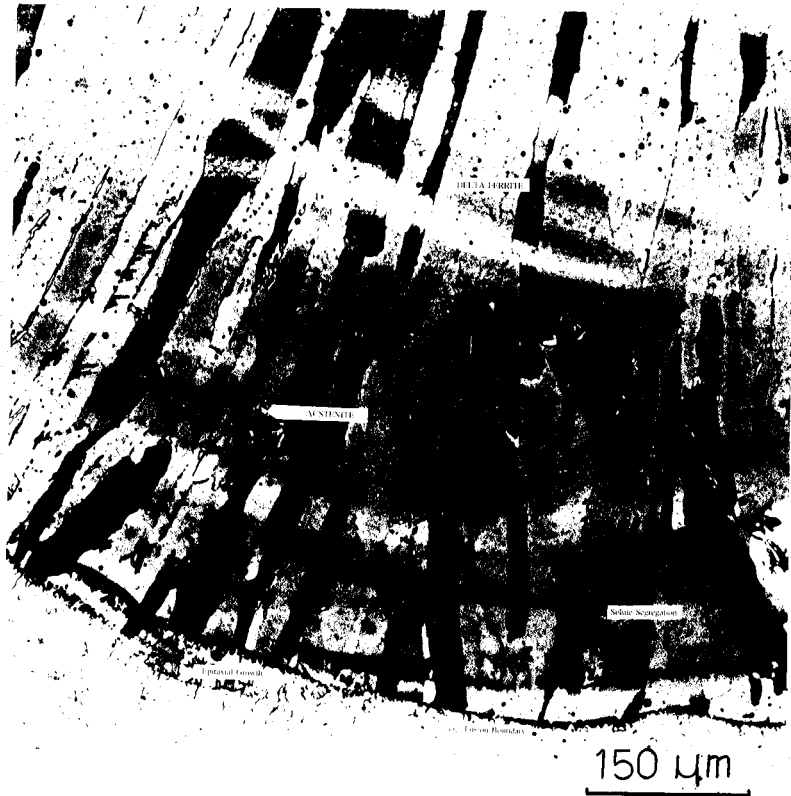
Figure 2.15. Nucleation of γ on prior δ grain boundaries.
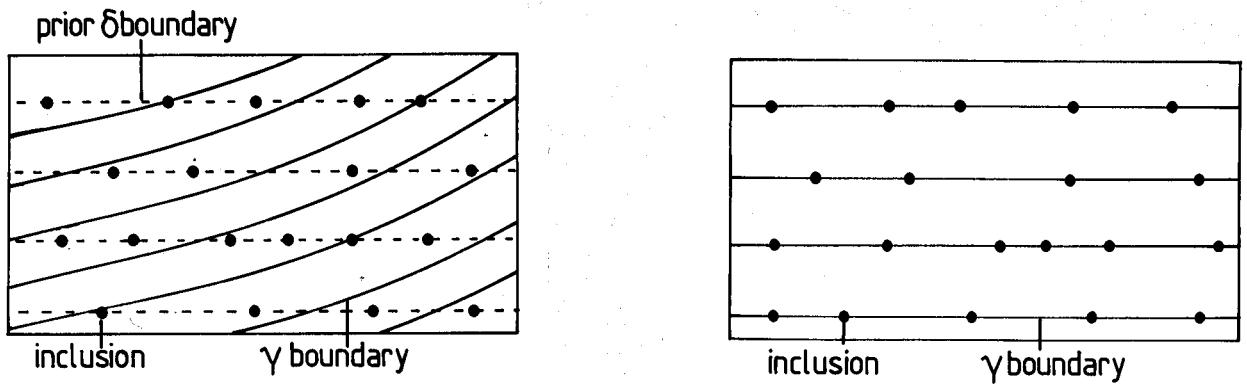
Figure 2.16. Schematic diagram showing solidification as prior δ (a) and γ (b). The δ and γ boundaries deviate in (a) as the thermal gradients are not constant in direction during cooling. Inclusions are assumed to segregate to solidification boundaries.

43

(a) grain boundary allotriomorphs

(b) Widmanstätten sideplates

(c) Widmanstätten sawteeth

(d) idiomorphs

(e) intragranular Widmanstätten plates

(f) massive structure
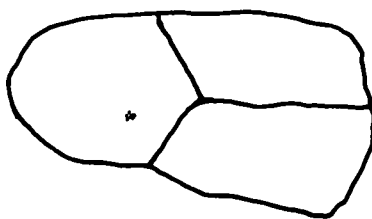
Figure 2.17. Dubé classification.

44
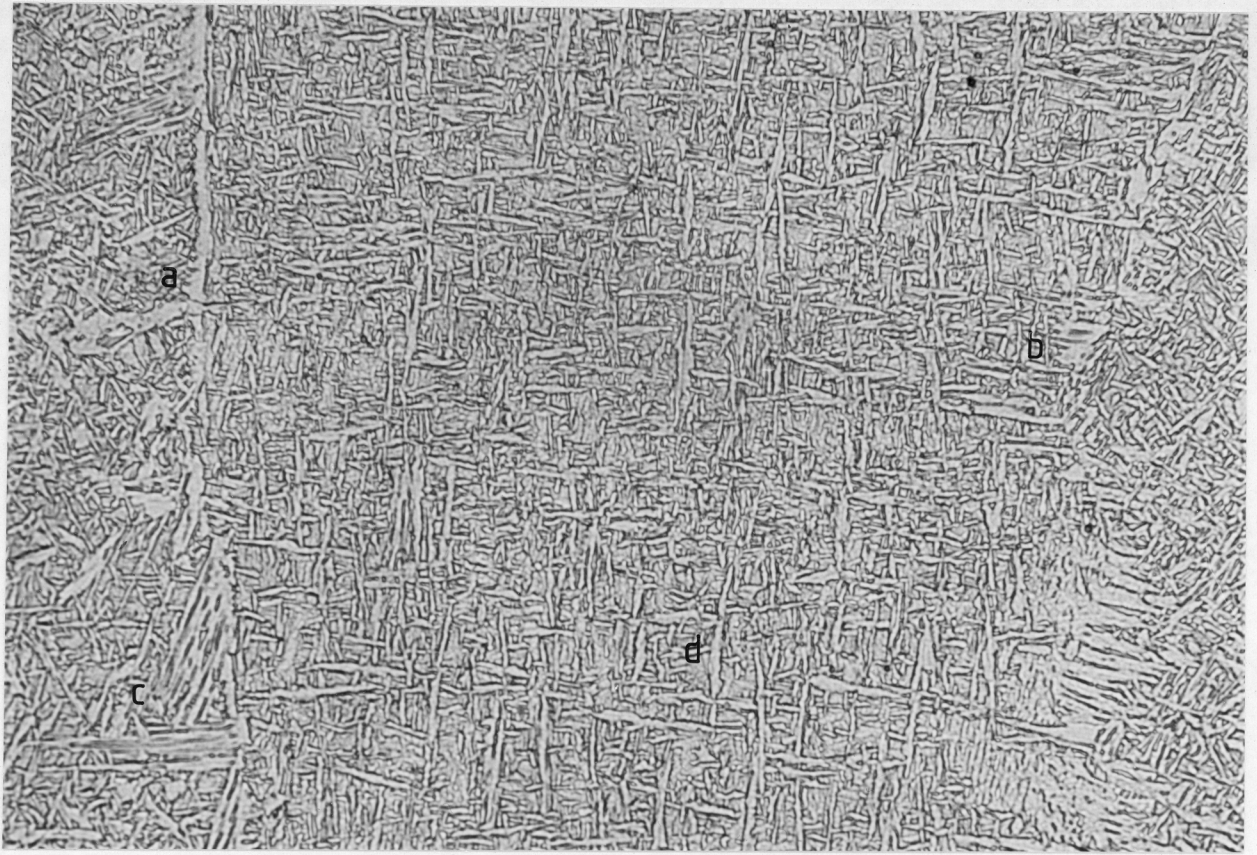
30 μm ⌐⎯⎯⌐

Figure 2.18. Weld metal microstructural features, (a) allotriomorphic ferrite, (b) primary Widmanstätten α sideplates, (c) secondary Widmanstätten α sideplates and (d) acicular ferrite.

low alloy content

high alloy content
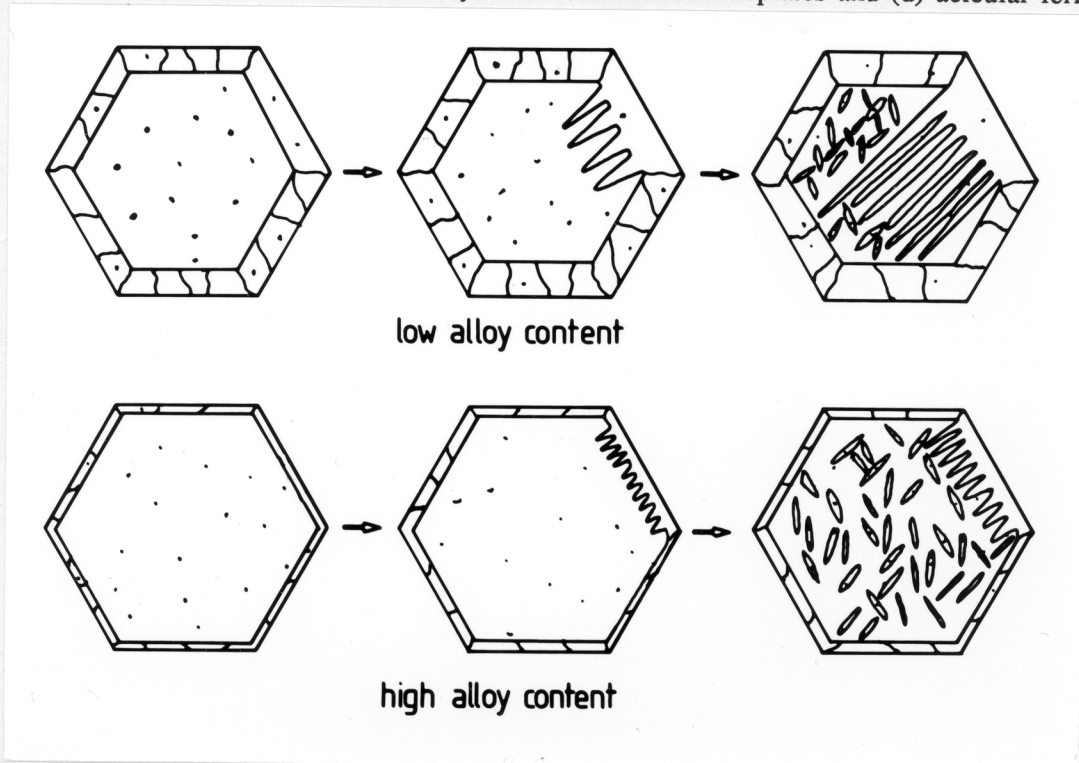
Figure 2.19. Development of ferrite phases in welds.

45
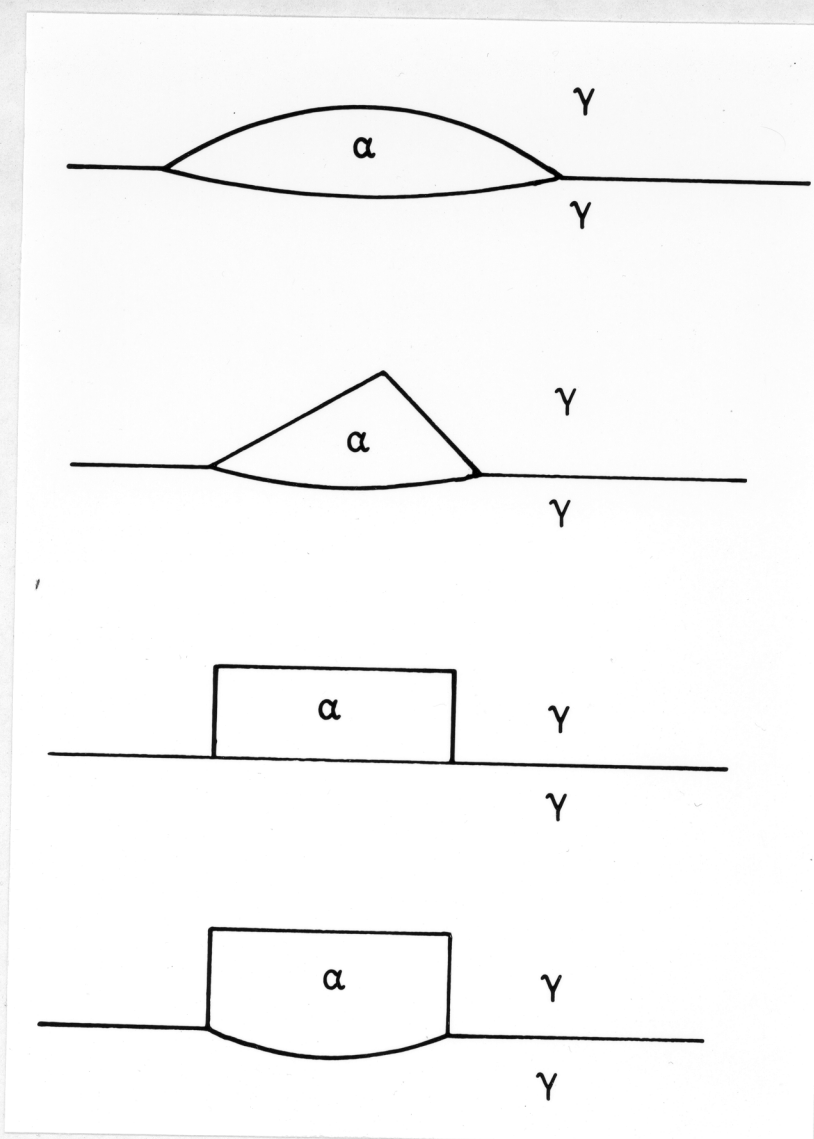
Figure 2.20. Various nuclei shapes.

3.0 μm └─────┘
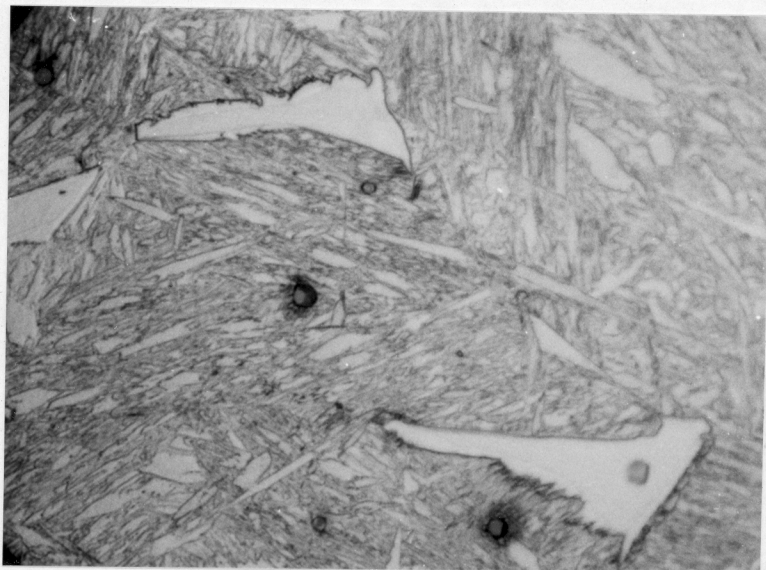
Figure 2.21. Facetted α allotriomorphs on prior γ grain boundaries.
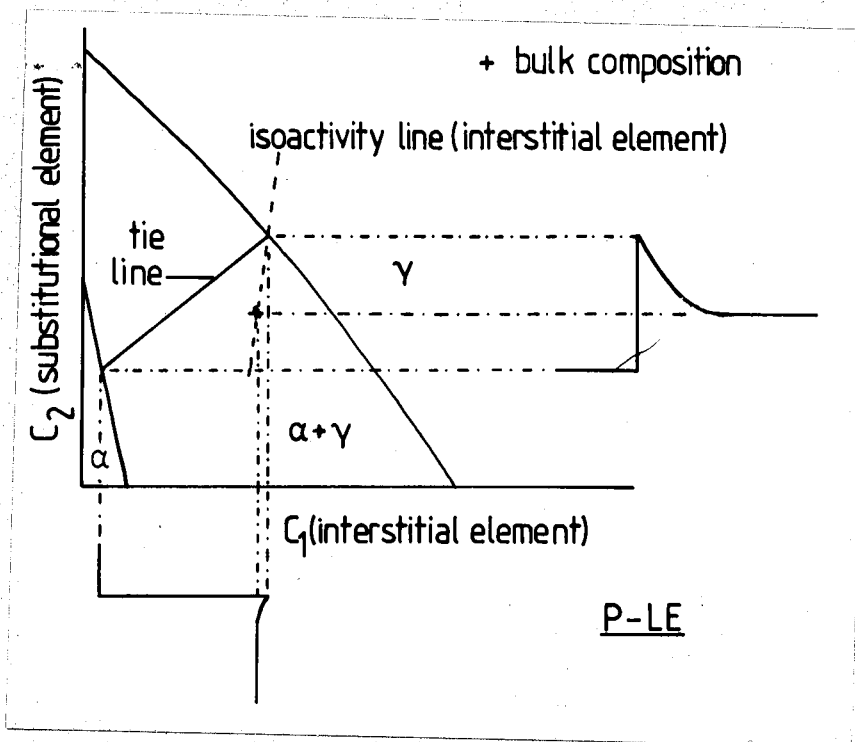
Figure 2.22. Isothermal section for P-LE.
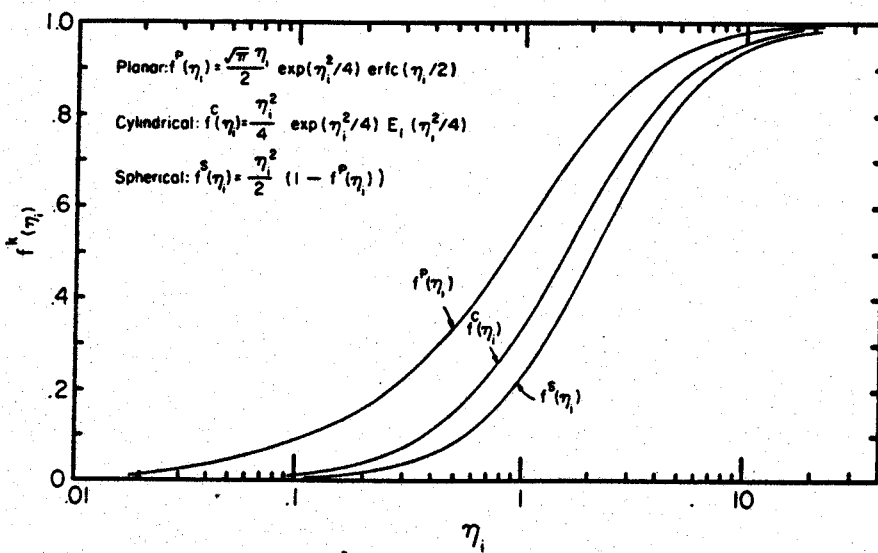
Figure 2.23. Relationship between fractional composition (f^k_i) and growth rate constant (η_i).

47
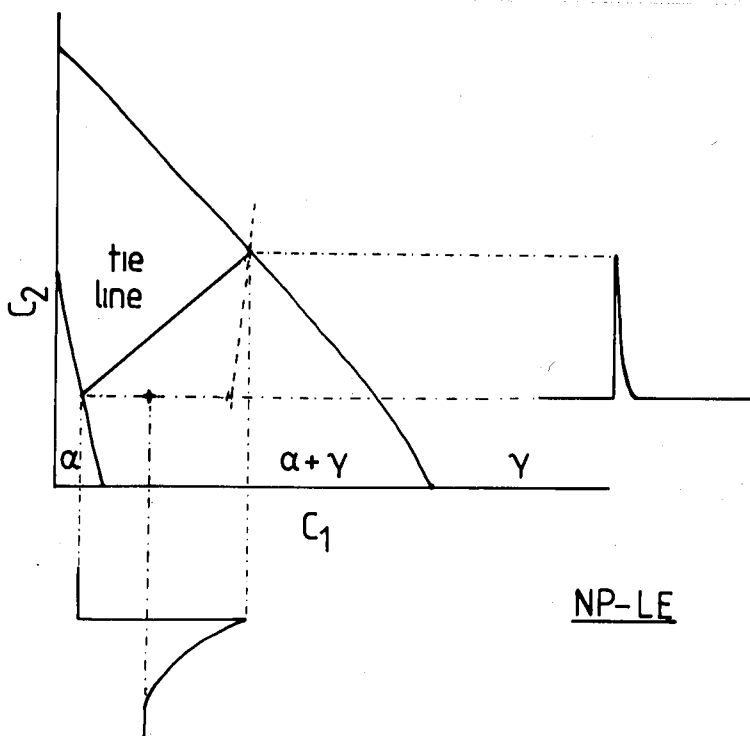
Figure 2.24. Isothermal section for NP-LE.
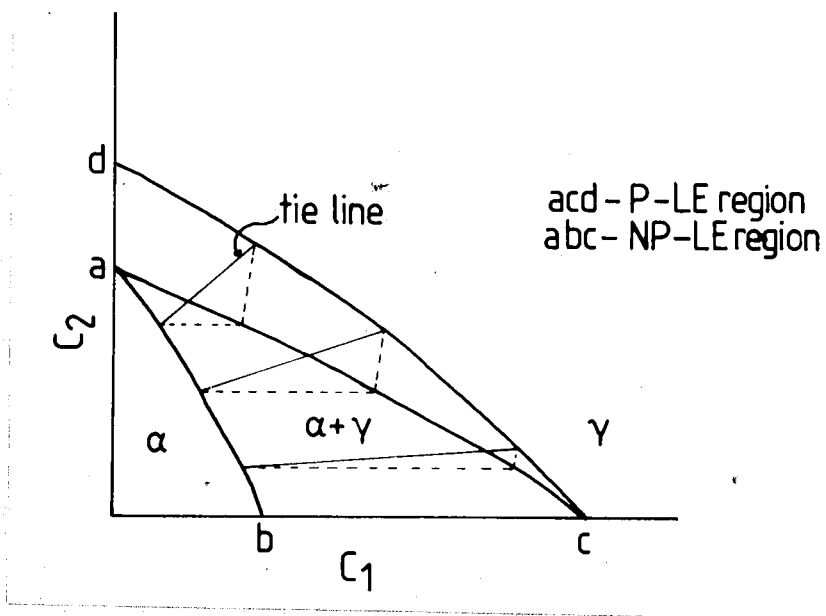
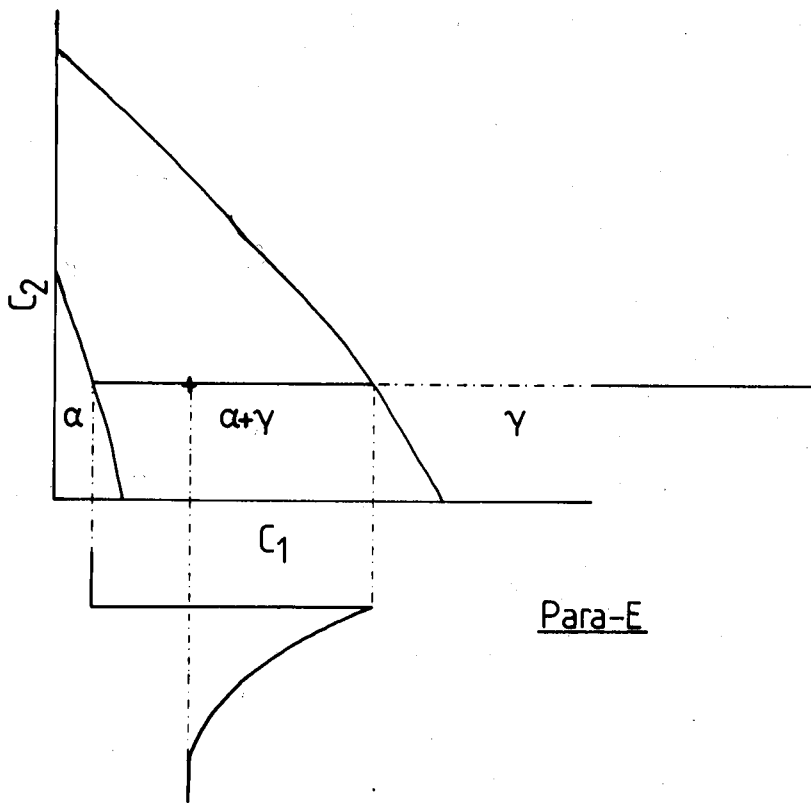Figure 2.25. Isothermal section showing regions of P-LE and NP-LE growth control.
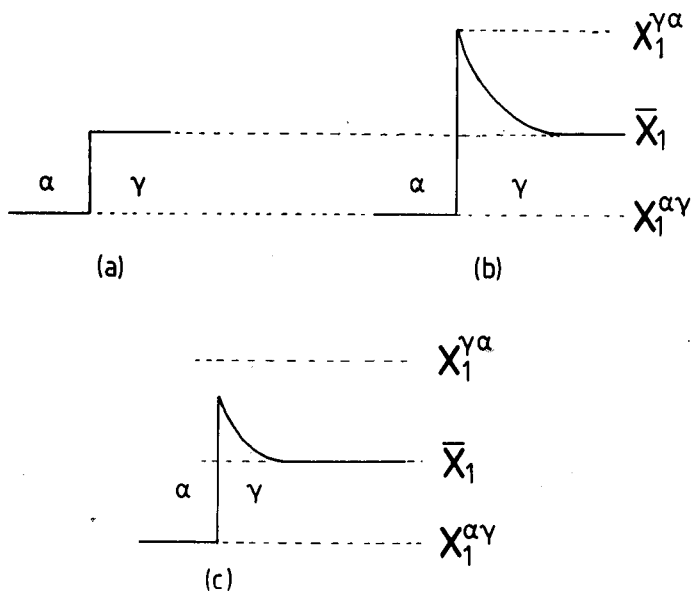
48

Figure 2.26. Isothermal section for ParaE growth.

Figure 2.27. Carbon distribution at interface during growth by (a) interface control, (b) diffusion control and (c) mixed control.

$\overline{X}_1$=bulk concentration, $X_1^{\gamma\alpha}$=concentration at $\gamma/(\gamma+\alpha)$ phase boundary, $X_1^{\alpha\gamma}$=concentration at $(\alpha+\gamma)/\alpha$ phase boundary.
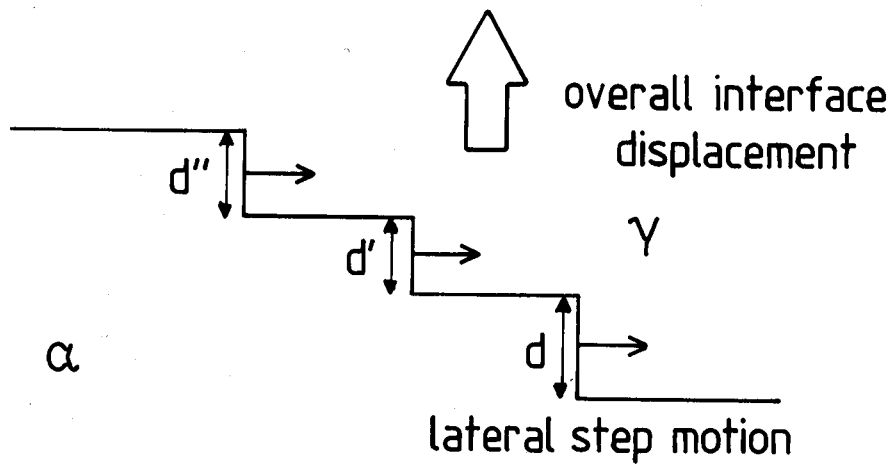
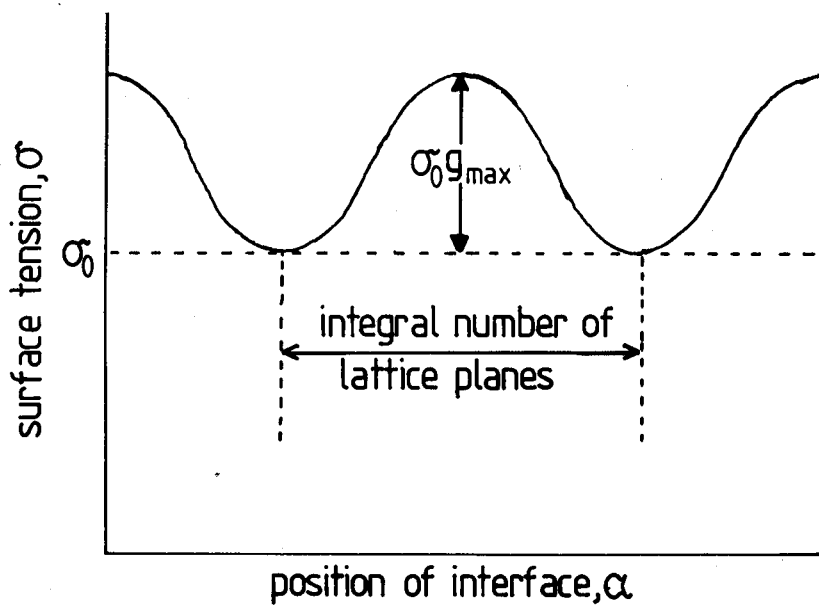Figure 2.28. Normal advance of interface by lateral passage of steps, height d.

Figure 2.29. Variation of σ with interface position.